Manuscript prepared for Atmos. Chem. Phys. Discuss.
with version 2014/09/16 7.15 Copernicus papers of the LaTeX class copernicus.cls.
Date: 14 March 2016

Validation of the Swiss methane emission inventory by atmospheric observations and inverse modelling

S. Henne[1], D. Brunner[1], B. Oney[1], M. Leuenberger[2], W. Eugster[3], I. Bamberger[3,4], F. Meinhardt[5], M. Steinbacher[1], and L. Emmenegger[1]

[1]Empa Swiss Federal Laboratories for Materials Science and Technology, Überlandstrasse 129, Dübendorf, Switzerland
[2]Univ. of Bern, Physics Inst., Climate and Environmental Division, and Oeschger Centre for Climate Change Research, Bern, Switzerland
[3]ETH Zurich, Inst. of Agricultural Sciences, Zurich, Switzerland
[4]Institute of Meteorology and Climate Research Atmospheric Environmental Research (IMK-IFU), Karlsruhe Institute of Technology (KIT), Garmisch-Partenkirchen, Germany
[5]Umweltbundesamt (UBA), Kirchzarten, Germany

Correspondence to: S. Henne (stephan.henne@empa.ch)

Abstract

Atmospheric inverse modelling has the potential to provide observation-based estimates of greenhouse gas emissions at the country scale, thereby allowing for an independent validation of national emission inventories. Here, we present a regional scale inverse modelling study to quantify the emissions of methane (CH_4) from Switzerland, making use of the newly established CarboCount-CH measurement network and a high resolution Lagrangian transport model. In our reference inversion, prior emissions were taken from the "bottom-up" Swiss Greenhouse Gas Inventory (SGHGI) as published by the Swiss Federal Office for the Environment in 2014 for the year 2012. Overall we estimate national CH_4 emissions to be $196 \pm 18\,\mathrm{Gg\,yr^{-1}}$ for the year 2013 (1σ uncertainty). This result is in close agreement with the recently revised SGHGI estimate of $206 \pm 33\,\mathrm{Gg\,yr^{-1}}$ as reported in 2015 for the year 2012. Results from sensitivity inversions using alternative prior emissions, uncertainty covariance settings, large-scale background mole fractions, two different inverse algorithms (Bayesian and extended Kalman Filter), and two different transport models confirm the robustness and independent character of our estimate. According to the latest SGHGI estimate the main CH_4 source categories in Switzerland are agriculture (78 %), waste handling (15 %) and natural gas distribution and combustion (6 %). The spatial distribution and seasonal variability of our posterior emissions suggest an overestimation of agricultural CH_4 emissions by 10 to 20 % in the most recent SGHGI, which is likely due to an overestimation of emissions from manure handling. Urban areas do not appear as emission hotspots in our posterior results suggesting that leakages from natural gas distribution are only a minor source of CH_4 in Switzerland. This is consistent with rather low emissions of $8.4\,\mathrm{Gg\,yr^{-1}}$ reported by the SGHGI but inconsistent with the much higher value of $32\,\mathrm{Gg\,yr^{-1}}$ implied by the EDGARv4.2 inventory for this sector. Increased CH_4 emissions (up to 30 % compared to the prior) were deduced for the north-eastern parts of Switzerland. This feature was common to most sensitivity inversions, which is a strong indicator that it is a real feature and not an artefact of the transport model and the inversion system. However, it was not possible to assign an unambiguous source process to the region. The observations of

the CarboCount-CH network provided invaluable and independent information for the validation of the national bottom-up inventory. Similar systems need to be sustained to provide independent monitoring of future climate agreements.

1 Introduction

Atmospheric methane (CH_4) acts as an important greenhouse gas (GHG) whose man-made increase from pre-industrial to present day levels (from $\approx 700\,\mathrm{nmol\,mol^{-1}}$ in 1750 to $1819\,\mathrm{nmol\,mol^{-1}}$ in 2012) directly and indirectly contributes 0.97 (0.74–1.20) $\mathrm{W\,m^{-2}}$ to present day global radiative forcing (Myhre et al., 2013). As such, its contribution to human-induced global warming is second only to carbon dioxide (CO_2). Globally, natural sources (wetlands, lakes, geological seeps, termites, methane hydrates, and wild animals) and anthropogenic sources (fossil fuel extraction, distribution and combustion, rice cultivation, ruminants, and waste) each contribute about half to CH_4 emissions to the atmosphere (Kirschke et al., 2013), but larger uncertainties are connected with the natural sources. Owing to increased research efforts in recent years, uncertainties associated with these fluxes have decreased on the global and continental scale (Kirschke et al., 2013, and references therein). However, there remain open questions about the contributing processes and their temporal and spatial distributions on the regional scale (Nisbet et al., 2014).

In many developed countries natural CH_4 sources are of limited importance (Bergamaschi et al., 2010) and anthropogenic emissions dominate. For example $\approx 98\,\%$ of Swiss CH_4 emissions are thought to be of anthropogenic origin (Hiller et al., 2014a). Owing to its comparatively short atmospheric lifetime ($\approx 10\,\mathrm{years}$) CH_4 has been classified as a short-lived climate pollutant, and reducing anthropogenic CH_4 emissions has become a promising target to lower near-term radiative forcing (Ramanathan and Xu, 2010; Shindell et al., 2012). However, the development of efficient mitigation strategies requires detailed knowledge of the source processes and the success of the mitigation measures should be monitored once put into action. The Kyoto protocol sets legally binding GHG emission reduction targets for Annex-1 countries and the United Nations Framework Convention on Climate

Change (UNFCCC) calls signatory countries to report their annual GHG emissions of CO_2, CH_4, nitrous oxide, sulphur hexafluoride, and halocarbons.

In Switzerland, the Federal Office for the Environment (FOEN) collects activity data and emission factors in the Swiss Greenhouse Gas Inventory (SGHGI) (FOEN, 2014, 2015) and annually reports emissions following IPCC guidelines (IPCC, 2006). According to this inventory, emissions from agriculture are the single most important source (161.5 $\mathrm{Gg\,yr^{-1}}$) in Switzerland, followed by waste handling (32.3 $\mathrm{Gg\,yr^{-1}}$) and fossil fuel distribution and combustion (12.1 $\mathrm{Gg\,yr^{-1}}$, all values refer to the 2015 reporting for the year 2012). Estimates following IPCC guidelines are derived bottom-up from source-specific information combined with activity data and other statistical data, all of which may contain considerable uncertainties. Anthropogenic CH_4 emissions in Switzerland originate from processes that may vary strongly on an individual basis (e.g., ruminants, manure handling, waste treatment). Hence, on the country level they are much more difficult to quantify than anthropogenic emissions of CO_2, which can be largely deduced from fuel statistics. As a consequence, the uncertainty assigned to total Swiss CH_4 emissions ($\pm$16 %) is much larger than that of CO_2 emissions ($\pm$3 %) (FOEN, 2015). According to the SGHGI, Swiss CH_4 emissions have decreased by about 20 % since 1990 (FOEN, 2015), but given the above uncertainties, these estimates require further validation, also in order to survey the effectiveness of the realised reduction measures. Furthermore, considerable differences exist between the SGHGI and other global and European scale inventories (e.g. EDGAR) both in terms of total amount and spatial distribution (Hiller et al., 2014a). Previous validation efforts of the Swiss CH_4 inventory were restricted to flux measurements either on the site scale focusing on a specific emission process (Eugster et al., 2011; Tuzson et al., 2010; Schroth et al., 2012; Schubert et al., 2012) or campaign based flight missions (Hiller et al., 2014b) and tethered balloon soundings (Stieger et al., 2015), mainly confirming estimates of the SGHGI on the local scale. In addition, mobile near-surface measurements were used to verify emission hot spots in a qualitative way (Bamberger et al., 2014). However, due to the limited number of studies and the focus on rather small areas it is very difficult to employ these results for the validation of national total emission estimates.

Such an independent validation of spatially resolved national inventory data can be achieved through inverse modelling yielding a top-down estimate that uses atmospheric observations of the target species together with transport modelling in order to optimally estimate the underlying emissions (Enting, 2002; Bergamaschi et al., 2005). Early inverse modelling studies of CH_4 focused on the global scale budget and relied on global flask sampling observations (e.g. Hein et al., 1997; Houweling et al., 1999; Bergamaschi et al., 2000; Dentener et al., 2003; Mikaloff Fletcher et al., 2004). Later studies also included continuous surface and airborne observations (e.g. Vermeulen et al., 1999; Bergamaschi et al., 2005, 2010; Chen and Prinn, 2006; Kort et al., 2010; Manning et al., 2011; Miller et al., 2013) and provide country specific emissions. For data sparse regions, the additional use of satellite retrieved CH_4 data in atmospheric inversions has recently helped reducing uncertainties (Meirink et al., 2008; Bergamaschi et al., 2013) and increased the ability to deduce emissions with higher spatial resolution (Wecht et al., 2014; Turner et al., 2015). However, such top-down estimates were usually not made for small countries and regions like Switzerland ($\approx$10 000 km^2), owing to the coarse spatial resolution of the inversion systems. Recent studies from the USA have shown large differences between national and regional bottom-up estimates and inverse modelling, predominantly detecting large emission underestimations in the bottom-up inventories (Wecht et al., 2014; Turner et al., 2015; Miller et al., 2013; McKain et al., 2015; Wennberg et al., 2012). These were mainly attributed to three major source processes: oil and gas extraction, ruminants, and natural gas distribution to the end user.

Here, we validate the bottom-up estimate of Swiss CH_4 emissions as given in the SGHGI by analysing continuous, near surface observations of CH_4 from the newly established, dense CarboCount-CH measurement network in central Switzerland (Oney et al., 2015) and two neighbouring sites. For the first time, we apply an inverse modelling framework with high spatial resolution ($<$10 km) to a relatively small area with considerable land surface heterogeneity and topographical complexity. Such modelling approaches have only recently become feasible through the use of high-resolution atmospheric transport simulations (e.g. for CH_4, Zhao et al., 2009; Jeong et al., 2012, 2013; McKain et al., 2015). The

main aim of the study is to provide an independent validation of the SGHGI in terms of national total emissions (FOEN, 2015), geographical (Hiller et al., 2014a) and temporal distribution. Results in the spatio-temporal distribution shall be used to draw conclusions on the estimates of individual source processes.

2 Data and methods

2.1 Observations

The CH_4 observations used in this study are those of the CarboCount-CH[1] network (BEO, LHW, FRU, GIM) located on the Swiss Plateau and those from two additional mountain sites: Jungfraujoch and Schauinsland (see Fig. 1, S1 in the Supplement and Table 1). The Swiss Plateau, the relatively flat area between the Alps in the south and Jura mountains in the north, covers only about one third of the area of Switzerland but is home to two thirds of the Swiss population and is characterized by intensive agriculture and extended urban and suburban areas. Approximately two thirds of the Swiss CH_4 emissions are thought to stem from this area (Hiller et al., 2014a). Oney et al. (2015) characterised the transport to the CarboCount-CH sites applying the same transport model as used here. They find that all four sites are mainly sensitive to emissions from most of the Swiss Plateau during summer day-time conditions, whereas sensitivities are more localised around the sites in winter, but still provide reasonable coverage of the targeted area of the Swiss Plateau.

The Beromünster (BEO) site is located on a hill in an intensively used agricultural area. It is surrounded mainly by croplands and to a smaller extent rangeland. The site itself consists of a 217 m high decommissioned radio transmission tower. Gas inlets and meteorological instrumentation are installed on the tower at 5 different heights above ground (12 to 212 m), whereas the gas analyser is located at the foot of the tower. A comprehensive description of the installation and the measurement system can be found in Berhanu et al. (2015). Here, only the observations from the topmost inlet height (212 m) were used, since this height

[1] http://www.carbocount.ch, last accessed 9 September 2015

showed the largest extent of the relative footprint and, hence, is least influenced by local sources (Oney et al., 2015).

Lägern Hochwacht (LHW) is a mountain top site on a very steep, west–east extending crest approximately 15 km north-west of and 400 m above the city centre of Zurich, the largest city in Switzerland. The site is surrounded by forest with average tree crown heights of 20 m close to the site. The gas inlet and meteorological instrumentation is mounted on a small tower of 32 m.

Früebüel (FRU) is another mountain site and located at 982 m a.s.l. above lake Zug on the south-eastern edge of the Swiss Plateau. Unlike Lägern-Hochwacht, the site is located on a mountain top plateau with a south-west aspect above lake Zug and with slightly more elevated areas to the south-east. The area around the site is used as rangeland and emissions from a local dairy farm may influence the observations. In contrast to the other sites, gas samples and meteorological observations are taken close to the surface (3 m above ground). A more detailed analysis of how the observations of this site are locally influenced and how they can be compared to observations from the close-by tall tower in BEO is given in Bamberger et al. (2015). Here we only note that the influence of local emissions that cannot be accounted for in the transport model needs to be filtered from the observational data before the use in inverse modelling. We did this by removing all data (10 min resolution) with low wind speeds ($< 3\,\mathrm{m\,s^{-1}}$) coming from the direction of the aforementioned farm (140 to 200°). These thresholds were determined by comparing differences between the observations of BEO (212 m), which exhibit less local influences, and FRU as a function of wind speed and direction at FRU.

At the Gimmiz site (GIM, 443 m a.s.l.) sample gases are drawn from a 32 m tall water tower. The surrounding area is flat and dominated by intensive agriculture, mostly vegetable farming and croplands. The area is a transformed wetland that used to be regularly flooded until the 1850s before the leveling of the river system (1868–1891) when also former wetlands were converted to agricultural lands (Schneider and Eugster, 2007). Although there are only two small farms in the direct vicinity, larger potential CH_4 sources are located in the town of Aarberg about 2.5 km to the south-east. Here a sugar refinery, operating

a large-scale waste water treatment plant (250 000 person equivalent), a compost and soil recycling facility, and a biogas reactor for electrical power generation are located. These local sources may not be represented sufficiently well in model simulations. Therefore and as in the case of FRU, observations from GIM were filtered by wind speed and direction, excluding all 10 min averages for which wind speeds were either below 2 m s^{-1} or coming from directions between 90 and 150 °. Again these thresholds were estimated by comparison to the observations at BEO.

Schauinsland (SSL, 1205 m a.s.l.) is a mountain top site in the Black Forest, Germany, to the north of the Swiss Plateau. As such it is usually situated above the stable nocturnal boundary layer of the surrounding, but at day-time it is affected by boundary layer air (Schmidt et al., 1996). The site is surrounded by forests and rangeland and no large CH_4 source is known in the direct vicinity. While not part of CarboCount-CH network, the observations from SSL provide additional constraints for the atmospheric inversion especially at mid-distance from the Swiss Plateau.

The high-altitude observatory Jungfraujoch (JFJ, 3580 m a.s.l.) is located in the northern Swiss Alps on a steep mountain saddle between the two mountains Jungfrau (4158 m a.s.l.) and Mönch (4099 m a.s.l.). Although JFJ is usually located in the free troposphere, it intermittently receives polluted boundary layer air both from sources north and south of the Alps (Zellweger et al., 2003; Henne et al., 2010; Tuzson et al., 2011). The intensity of these transport events from the boundary layer can vary strongly depending on the weather condition and the transport process responsible for lifting.

At all sites CH_4 measurements were carried out using PICARRO (Santa Clara, CA, USA) cavity ring-down spectrometers (Rella et al., 2012) which provide high frequency (approximately 0.5 to 1 Hz) observations of CO_2, CH_4, H_2O and (at BEO and LHW) CO. All instruments were calibrated against the WMO X2004 CH_4 scale (Dlugokencky et al., 2005) and were reporting dry air mole fractions by either applying a water vapor correction accounting for dilution and spectroscopic effects (CarboCount-CH sites and SSL) or by using presample drying of sample air (JFJ). At the CarboCount-CH sites, measurements of additional target gases, not used for the calibration, give an estimate of the instruments' non-random

uncertainty for CH_4 of $\approx 0.5\,\mathrm{nmol\,mol^{-1}}$ (Oney et al., 2015). At SSL observations of three additional target gases yield a combined measurement uncertainty of $0.3\,\mathrm{nmol\,mol^{-1}}$. For JFJ a combined measurement uncertainty of $\sigma = \sqrt{0.31^2 + (3.61 \times 10^{-4} \times \chi)^2}\,\mathrm{nmol\,mol^{-1}}$ was reported for hourly aggregates, where χ is the observed mole fraction (Empa, 2015).

For the use in the inversion 3 hourly aggregates were produced from high frequency observations for the period 1 March 2013 to 28 February 2014, the first year with a complete set of measurements for all CarboCount-CH sites. Prior to aggregation, the data filtering as described above was applied to the sites GIM and FRU. Out of the dataset, only the afternoon values, covering 12:00 to 18:00 UTC (CarboCount-CH sites), were used in the atmospheric inversion. This was done in order to capture the time of day with the deepest planetary boundary layer (PBL) extent, which should also be best captured by the transport model and yield the smallest model bias (Kretschmer et al., 2014) and at the same time minimise the influence of local sources and sinks. For the elevated sites JFJ and SSL, the night-time data from 00:00 to 06:00 UTC were used instead. This is the time when the sites are least influenced by small-scale, thermally induced flow systems in the complex topography around the sites. Since the sites are situated on mountain tops no development of a shallow night-time boundary layer is expected so that the influence of local sources (if at all present) remains negligible at night. All of the following analysis and discussion is based on this filtered and aggregated dataset. In addition to the absolute mole fraction, an estimate of larger-scale background mole fractions, which represent conditions without recent emission input, was generated using the "Robust Estimation of Baseline Signal" (REBS) method (Ruckstuhl et al., 2012). We refer to this term as baseline mole fraction in the following. It represents a smooth curve fitted to the data, providing a baseline mole fraction for each observational time. The absolute mole fraction of the observations, χ_{o}, can then be given as the sum of the baseline, $\chi_{o,\,b}$, and the contribution due to recent emissions, $\chi_{o,\,p}$,

$$\chi_{o} = \chi_{o,\,p} + \chi_{o,\,b}. \tag{1}$$

The REBS method iteratively fits a non-parametric local regression curve to the observations, successively excluding points outside a certain range around the baseline curve. REBS was applied separately to hourly data from each site using asymmetric robustness weights with a tuning factor of $b = 3.5$, a temporal window width of 60 days and a maximum of 10 iterations. An estimate of the baseline uncertainty is given by REBS as a constant value for the whole time series. For JFJ the baseline uncertainty was estimated to 17.4 nmol mol^{-1}, whereas uncertainties for the other sites ranged between 16.2 nmol mol^{-1} (SSL) and 18.9 nmol mol^{-1} (LHW). The larger values generally reflect a larger degree of variability in the baseline and a reduced frequency of air masses not influenced by recent surface contact and emissions.

2.2 Transport models

Source sensitivities giving the direct influence of a mass emission from a source location onto the mole fraction at a receptor site were calculated with two different versions of the Lagrangian Particle Dispersion Model (LPDM) FLEXPART (Stohl et al., 2005), which can be run in time-inverted mode. The first represents the standard FLEXPART model (version 9.02) driven by analysis fields of the operational runs of the Integrated Forecast System (IFS) of the European Centre for Medium Range Weather Forecast (ECMWF). Input fields were available every 3 h with a horizontal resolution of 0.2° × 0.2° (≈ 15 km × ≈ 22 km) for the Alpine area (-4°E to 16°E and 39°N to 51°N) and 1° × 1° elsewhere. The second FLEXPART version is the one adapted to the use of output from the COSMO regional numerical weather prediction (NWP) model (Baldauf et al., 2011). FLEXPART-COSMO was driven by operational analysis fields as generated hourly by the Swiss national weather service, MeteoSwiss, for Western Europe (approx. -10°E to 20°E and 38°N to 55°N) with a horizontal resolution of approx. 7 km × 7 km. Hourly analysis fields are produced applying an observational nudging technique (Schraff, 1997) to near surface and vertical profile observations of pressure, relative humidity and wind. The use of a high-resolution transport model in regional scale inversions based on point observations is a prerequisite to reduce the representation uncertainty of the model (Tolk et al., 2008; Pillai et al., 2011). Furthermore,

the use of a time-inverted LPDM is highly beneficial to this purpose as it allows an accurate transport description in the near-field of the sites below the resolution of the driving meteorology.

The main differences between FLEXPART-COSMO and standard FLEXPART-ECMWF are the internal vertical grid representation and the parameterisation of convective transport. In FLEXPART-COSMO, the native vertical grid of the COSMO model is used as the main frame of reference, which, in this case, was a height-based hybrid coordinate system (Gal-Chen and Somerville, 1975). In contrast, standard FLEXPART uses a terrain-following vertical coordinate with constant level depths up to the model top, which requires an initial vertical interpolation from the pressure-based hybrid coordinate used in the IFS. In FLEXPART-COSMO, all interpolation to particle positions is done directly from the native COSMO grid, avoiding multiple interpolation errors. In FLEXPART-ECMWF sub-grid scale convection is treated by an Emanuel type scheme (Emanuel and Zivkovic-Rothman, 1999; Forster et al., 2007), whereas in FLEXPART-COSMO the same modified version of the Tiedtke convection scheme (Tiedtke, 1989) as used in COSMO was implemented.

PBL heights are a critical parameter in FLEXPART since they are used as a scaling parameter for the turbulence parameterisation. We use the default implementation within FLEXPART to diagnose PBL heights applying a Bulk-Richardson method (Stohl et al., 2005; Vogelezang and Holtslag, 1996). In contrast to standard FLEXPART we did not use 2-metre temperatures from COSMO in the PBL estimation but the lowest model level temperature (approx. 10 m above ground), because FLEXPART and COSMO PBL heights showed a positive bias when compared to PBL height observations from the sounding site Payerne on the Swiss Plateau under convective conditions and when using 2-metre temperatures (Collaud Coen et al., 2014). This bias disappeared when using the first level temperatures instead.

With both model versions source sensitivities were calculated for each observation site and 3 hourly interval. For each interval and location a total of 50 000 particles was released and followed backward in time for 4 and 10 days in the COSMO and ECMWF version, respectively. Particles leaving the limited COSMO-7 domain were terminated prematurely.

The limited horizontal model resolution and the complex terrain in the investigated domain lead to differences between the model surface altitude and the real site altitude. In such situations, the most representative height above model ground for particle releases in an LPDM is not well known. Therefore, we chose to release particles at two vertical locations for the CarboCount-CH sites to analyse the sensitivity of this choice. At BEO, where the model topography is relatively close to the site's altitude, these span the possible range of reasonable release altitudes by representing (1) the height above model surface as given by the inlet height of the observations and (2) the absolute altitude above sea level of the inlet. At the sites FRU and LHW the lower release height was chosen 50 m and the higher 150 m above model ground because height deficiencies in the model were larger here. At GIM only one release height was used because the model topography was relatively close to the true surface altitude. Also for the more remote sites JFJ and SSL only one release height was simulated that represents the middle between the model surface and the site altitude. Previously it was shown that such an approach works best (independent of time of day) for the mountaintop site JFJ, which shows large model topography deficits (Brunner et al., 2013). Values for all release heights are given in Table 1. Note that release heights were the same for all FLEXPART-ECMWF and FLEXPART-COSMO simulations except for JFJ and SSL were surface height differences between the models were large.

From both models, output was generated on a regular longitude/latitude grid with a horizontal resolution of $0.16^\circ \times 0.12^\circ$ (≈ 13 km) covering Western Europe and for a nested Alpine domain with a horizontal resolution of $0.02^\circ \times 0.015^\circ$ (≈ 1.7 km). The generated output represents the summed residence time, $\tau_{i,j}$, of particles in a given grid box, i, j, and below a specific sampling height, h_s, divided by the density of dry air in this grid cell and has units $\mathrm{s\,m^3\,kg^{-1}\,gridcell^{-1}}$. The sampling height was set to 50 and 100 m above ground in FLEXPART-COSMO and FLEXPART-ECMWF, respectively, coinciding with the minimal PBL height used in the models. Multiplication of $\tau_{i,j}$ with the volume of the sampling grid cell, $V_{i,j} = A_{i,j} \cdot h_\mathrm{s}$, and the ratio of the molar weight of the species of interest, μ_s, and the molar

weight of dry air, μ_{d}, yields the desired source sensitivity, $m_{i,j}$, in units $\mathsf{s\,kg^{-1}\,mol\,mol^{-1}}$

$$m_{i,j} = \frac{\tau_{i,j}}{V_{i,j}} \frac{\mu_{\mathsf{d}}}{\mu_{\mathsf{s}}}. \tag{2}$$

$m_{i,j}$ multiplied by a mass emission in a grid box (i,j), $E_{i,j}$ ($\mathsf{kg\,s^{-1}}$) gives the effect this emission would have on the dry air mole fraction at the receptor. The sum over all grid boxes then yields the increase in mole fraction, χ_{p}, due to recent emissions, whereas the baseline mole fraction, χ_b, can be obtained as the average mole fraction over all particles at their endpoints in the simulation

$$\chi = \underbrace{\sum_{i,j} m_{i,j} E_{i,j}}_{\chi_p} + \underbrace{\frac{1}{K} \sum_{k}^{K} \chi_k}_{\chi_b}, \tag{3}$$

where i,j are the horizontal grid indices, χ_k the mole fraction at each particle's end point, and K is the number of particles. In our FLEXPART-COSMO simulations particles were followed for 4 days backward in time. Not all particles leave the limited area model domain during this time, so that the baseline mole fraction as given in (3) cannot be directly translated to conditions at the domain boundaries, but may also contain contributions from within the domain and, therefore, may vary between different sites. For the inversion set-up it would be beneficial if the baseline mole fractions could be estimated from an external 3-dimensional model. However, such model input was not available at the time of analysis, and thus the prior baseline mole fraction was taken as the one estimated from the observations (REBS) and further optimised in the inversion.

2.3 Inversion framework

In our inversion system the source sensitivities calculated by the transport model can be used to give a direct relationship between the simulated mole fractions and the so called

state vector, $\boldsymbol{x} = (x_1 \dots x_K)$ with a total of K elements, that primarily contains the desired gridded emissions. In matrix notation this can be expressed as

$$\boldsymbol{\chi} = \mathbf{M}\boldsymbol{x}, \tag{4}$$

where $\boldsymbol{\chi} = (\chi_1 \dots \chi_L)$ represents the simulated mole fractions at different times and locations, $l = 1, \dots, L$. The sensitivity matrix $\mathbf{M}$ (dimensioned $K \times L$) contains the sensitivities for each time/location towards the kth element of the state vector.

In our case, the state vector contained additional parameters characterising the baseline mole fractions χ_b at different times and for different sites. Hence, $\boldsymbol{x}$ contained K_E elements describing the emissions and $K_\mathrm{B} = K - K_\mathrm{E}$ elements giving baseline mole fractions, which were not estimated at each observation but at discrete time intervals (baseline nodes). Therefore, the sensitivity matrix $\mathbf{M}$ consists of two block matrices $\mathbf{M}^\mathrm{E}$ and $\mathbf{M}^\mathrm{B}$ giving the dependence on the emissions and baseline mole fractions, respectively. Similar to Stohl et al. (2009), elements of $\mathbf{M}^\mathrm{B}$ were set to represent temporal linear interpolation between the baseline mole fractions at the neighbouring baseline nodes. We estimate the baseline separately for each site in the inversion, since it does not necessarily just reflect the conditions at the boundary of the domain, but may also contain contributions from within the domain (see discussion above). Different sites may therefore have different levels of within-domain-influence. This is especially true for sites at different altitudes even if these are located at short distances as in our network. Since the baseline treatment is a critical part of the inversion system and may lead to attribution errors of the emissions, we present two alternative baseline estimation approaches as part of our sensitivity analysis (see Sect. 2.5.7). For our base inversion, baseline nodes were spaced equidistantly with a distance of $\tau_\mathrm{B} = 5$ days over the observation period and were optimised separately for each site, resulting in 73 baseline elements in the state vector for each site. Prior estimates of the baseline mole fractions were REBS estimates for the site JFJ (see Sect. 2.1). Since the REBS estimate represents a smooth curve to the data, the REBS value at the time of a given baseline node was used as its prior value.

In our base set-up we target temporal average emission fluxes for the period of observations (March 2013 to February 2014) and optimise their spatial distribution. We include seasonality in the emission fluxes as part of our sensitivity analysis (see Sect. 2.5.2).

In order to reduce the size of the inversion problem, emissions were not optimised on a regular longitude/latitude grid as given by the FLEXPART simulations. Instead, a reduced grid was used that assigns finer (coarser) grid cells in areas with larger (smaller) average source sensitivities. Starting from the finest output grid resolution of $0.02^\circ \times 0.015^\circ$ four neighbouring grid cells were merged if their average residence time did not reach a specified threshold. This procedure was iterated up to a maximum grid cell size of $2.56^\circ \times 1.92^\circ$. The residence time threshold was set manually in order to reduce the number of cells in the inversion to the order of $K_\mathrm{E} \approx 1000$. The overall extent of the emission grid was determined by (1) the extent of the COSMO-7 domain, (2) the existence of considerable CH_4 emissions (cut-off over the oceans) and (3) a minimum source sensitivity. Tests with larger and smaller inversion domains did not indicate significant influences on the deduction of Swiss emissions.

In Bayesian atmospheric inversion prior knowledge of the state vector, $\boldsymbol{x}_b$, and its probability distribution is used to guide the optimisation process. Mathematically this can be expressed by formulating a cost function J that penalises deviations from the prior state and differences between simulated and observed mole fractions (e.g. Tarantola, 2005)

$$J = \frac{1}{2}\left(\boldsymbol{x} - \boldsymbol{x}_\mathrm{b}\right)^T \mathbf{B}^{-1}\left(\boldsymbol{x} - \boldsymbol{x}_\mathrm{b}\right) + \frac{1}{2}\left(\mathbf{M}\boldsymbol{x} - \boldsymbol{\chi}_\mathrm{o}\right)^T \mathbf{R}^{-1}\left(\mathbf{M}\boldsymbol{x} - \boldsymbol{\chi}_\mathrm{o}\right), \tag{5}$$

where $\boldsymbol{x}$ describes the optimised and $\boldsymbol{x}_b$ the prior state vector, and $\mathbf{M}\boldsymbol{x} - \boldsymbol{\chi}_\mathrm{o}$ is the difference between simulated and observed mole fractions. **B** and **R** give the uncertainty covariance matrices of the prior state and the combined model-observation uncertainty. In Sect. 2.4 the structure of these matrices is discussed in more detail. Minimisation of J yields the posterior state

$$\boldsymbol{x} = \boldsymbol{x}_\mathrm{b} + \mathbf{B}\mathbf{M}^T\left(\mathbf{M}\mathbf{B}\mathbf{M}^T - \mathbf{R}\right)^{-1}\left(\boldsymbol{\chi}_\mathrm{o} - \mathbf{M}\boldsymbol{x}_\mathrm{b}\right). \tag{6}$$

In our implementation the inverse of $\mathbf{S} = \left(\mathbf{MBM}^T - \mathbf{R}\right)$, a $L \times L$ matrix, was calculated using LU factorisation (function DGESVX in LAPACK). In addition to the posterior state also its uncertainty expressed as an uncertainty covariance matrix, $\mathbf{A}$, can be given (e.g. Tarantola, 2005)

$$\mathbf{A} = \mathbf{B} - \mathbf{BM}^T\mathbf{S}^{-1}\mathbf{MB}. \quad (7)$$

The total emissions and their uncertainty from a certain region or country can then be calculated as

$$E = \sum_{k}^{K_{\mathsf{E}}} x_k g_k; \sigma_{\mathsf{E}}^2 = \boldsymbol{g}^T \mathbf{A}^{\mathsf{E}} \boldsymbol{g}, \quad (8)$$

where the vector $\boldsymbol{g}$ gives the fractional contribution of a region to an inversion grid cell and $\mathbf{A}^{\mathsf{E}}$ is the part of $\mathbf{A}$ that contains the uncertainty covariance of the posterior emissions. g_k takes a value of 1 for a grid cell that is completely within the region and 0 for grid cells outside the region. For coarse inversion grid cells containing more than one region, g_k was calculated from higher resolution population data, weighting per region contributions by population and not by land surface area. In the case of the present CH_4 inversion and the national estimates for Switzerland this treatment was of minor importance but is more crucial for other species that exhibit sharp emission gradients more closely following the population distribution (e.g., halocarbons).

In our base inversion, we used the Swiss MAIOLICA inventory (Hiller et al., 2014a), which is based on the total Swiss emissions estimated by FOEN (SGHGI) for the year 2011 and reported to UNFCCC in 2013. For areas outside Switzerland prior emissions were taken from the European scale inventory developed by TNO for the MACC-2 project (Kuenen et al., 2014) (TNO/MACC-2 hereafter) applying the same country-by-country scaling to 2011 values reported to UNFCCC in 2013.

2.4 Covariance design

This section details the construction of the uncertainty covariance matrices **B** and **R** as used in the base inversion. Parameters used to build the matrices were chosen based on experience and previous publications (see below). The sensitivity to these choices was investigated in a set of sensitivity inversions as described in Sect. 2.5.

Both uncertainty covariance matrices are symmetric block matrices. In the case of **B** one block, $\mathbf{B}^{\mathsf{E}}$, describes the uncertainty covariances of the emission vector and a second block, $\mathbf{B}^{\mathsf{B}}$, the uncertainty covariances of the baseline mole fractions. Within each block the off-diagonal elements were allowed to be non-zero. The diagonal elements of $\mathbf{B}^{\mathsf{E}}$ were set proportional (factor f_{E}) to the prior emissions in the respective grid cell $B^{\mathsf{E}}_{j,j} = (f_{\mathsf{E}} x_{b,j})^2$. For land grid cells with low emissions (below 10 % of land average) and ocean grid cells the uncertainty was set to 10 % of the average land cell uncertainty in order to avoid near zero uncertainties. Lacking more detailed information of the spatial uncertainty covariance structure, a spatial correlation of the uncertainty was assumed for the off-diagonal elements that decays exponentially with the distance between two grid cells (e.g., Rödenbeck et al., 2003; Gerbig et al., 2006; Thompson and Stohl, 2014)

$$B^{E}_{i,j} = e^{-\frac{d_{i,j}}{L}} \sqrt{B^{\mathsf{E}}_{i,i}} \sqrt{B^{\mathsf{E}}_{j,j}}, \tag{9}$$

where $d_{i,j}$ is the distance between two grid cell centres and L the correlation length. In this set-up the total squared uncertainty of the prior emissions $\sigma^2_{\mathsf{E}} = 1^T \mathbf{B}^{\mathsf{E}} 1$, where 1 is a vector of all ones, only depends on the settings of L and f_{E}. For the base inversion L was fixed to 50 km and f_{E} was adjusted to yield fixed relative uncertainties of the national estimate for Switzerland of 16 %, which is the uncertainty given for the Swiss bottom-up estimate (FOEN, 2015). The choice of 50 km was driven by the need for sufficient constraints for neighbouring grid cells, whereas Hiller et al. (2014a) suggested a shorter length scale around 10 km based on a comparison of the spatial structures of the MAIOLICA, TNO/MACC-2 and EDGAR CH_4 inventories.

All diagonal elements of $\mathbf{B}^{\mathsf{B}}$ were set to a constant value, $B^{\mathsf{B}}_{i,i} = f_{\mathsf{b}}\sigma^2_{\mathsf{b}}$, where σ_{b} is an estimate of any given baseline uncertainty and f_{b} is a scaling factor. The off-diagonal elements were set assuming an exponentially decaying correlation of the baseline uncertainty between baseline nodes at a given site

$$B^{\mathsf{B}}_{i,j} = e^{-\frac{T_{i,j}}{\tau_{\mathsf{b}}}}\sqrt{B^{\mathsf{B}}_{i,i}}\sqrt{B^{\mathsf{B}}_{j,j}}, \tag{10}$$

where $T_{i,j}$ is the time difference between two nodes and τ_{b} is the temporal correlation length. In the base inversion, σ_{b} was obtained from the REBS fit of the JFJ observations (17.4 nmol mol^{-1}), f_{b} was set to unity, and τ_{b} to 14 days. As for L, the choice of τ_{b} is somewhat arbitrary but governed by the need for sufficient constraints on the posterior solution without restricting adjustments too strongly .

In the case of temporally variable emissions (see Sect. 2.5.2) the state vector x, the sensitivity matrix and the prior uncertainty matrix have to be extended. $\mathbf{B}^{\mathsf{E}}$ now should treat spatial and temporal covariance of the state vector. Individual diagonal elements of $\mathbf{B}^{\mathsf{E}}$, $B^{\mathsf{E}}_{i,i}$, now refer to different emission locations and time, with the index i running over both of these dimensions. The off-diagonal elements can then be given by

$$B^{E}_{i,j} = e^{-\frac{T_{i,j}}{\tau_{\mathsf{t}}}}e^{-\frac{d_{i,j}}{L}}\sqrt{B^{\mathsf{E}}_{i,i}}\sqrt{B^{\mathsf{E}}_{j,j}}, \tag{11}$$

where in addition to equation (9), $T_{i,j}$ gives the time difference between two emission sets and τ_{t} is the temporal correlation length scale of the prior emissions.

The block matrix $\mathbf{R}$ contains one block for each site used in the inversion. In its diagonal elements both the observation and the model uncertainty were considered by quadratic addition

$$R_{i,i} = \sigma^2_{\mathsf{o}} + \sigma^2_{\mathsf{min}} + \sigma^2_{\mathsf{srr}}\chi^2_{\mathsf{p},i}, \tag{12}$$

where σ_o is the observation uncertainty as estimated for each 3 hourly CH_4 average (see Sect. 2.1) and the second and third term are contributions of the model uncertainty. σ_{min} represents a constant contribution while the third term represents an uncertainty contribution

relative to the prior simulation of above-baseline concentrations, $\chi_{\mathrm{p},i}$ (Brunner et al., 2012). For the base inversion, σ_{min} and σ_{srr} were estimated separately for each site from the model residuals (difference between simulated and observed mole fraction) of the prior simulation, $\chi_{\mathrm{p},i}$, by fitting a straight line through RMSEs calculated for separate bins along $\chi_{\mathrm{p,\,o}}$. The choice of this method was motivated by the observation that prior model residuals tend to increase with prior mole fractions. Estimating the model uncertainty from the prior model residuals has been suggested before by Stohl et al. (2009), where σ_{min} was estimated as the RMSE from the prior simulation, whereas σ_{srr} was set to 0. In an additional step this constant value was then forced to yield a normal distribution of the normalised model residuals. Furthermore, Stohl et al. (2009) applied their uncertainty estimation in an iterative way using the model residuals from successive inversion runs. In our experience this may lead to underestimated model uncertainties and we did not iterate our procedure. These methods have in common that the results of the prior simulation influence the estimation of R, therefore somewhat violating the independence of prior and model/observation uncertainties assumed in the Bayesian approach. Finally, off-diagonal elements of the model-observations uncertainty covariance matrix were assumed to follow an exponentially decaying correlation structure.

$$R_{i,j} = e^{-\frac{T_{i,j}}{\tau_{\mathrm{o}}}} \sqrt{R_{i,i}} \sqrt{R_{j,j}}, \tag{13}$$

where $T_{i,j}$ is the time difference between two measurements and τ_{o} is the temporal correlation length that describes the auto-correlation in the model-observation uncertainty. In the base inversion τ_{o} was set to 0.5 days, a value previously used by other authors (e.g. Thompson et al., 2011) and associated with the inability of atmospheric transport models to correctly simulate the diurnal cycle in the PBL. The uncertainty covariances between observations from different sites were set to 0.

2.5 Sensitivity inversions

The Bayesian inversion provides an estimate of the posterior uncertainty of the state vector, which in itself should be sufficient to give an estimate of the combined top-down un-

certainty. However, this analytical uncertainty tends to underpredict the true uncertainty. Optimality of the Bayesian approach requires normally distributed probability density functions, temporally uncorrelated residuals, and non-systematic uncertainties; requirements that are difficult to meet exactly in practice. In particular, potential systematic uncertainties in model transport, which may contribute importantly to the overall uncertainty (e.g. Gerbig et al., 2008), are not accounted for. To explore the range of uncertainty beyond the analytically derived posterior uncertainty and to test the robustness of the results to different assumptions, it has therefore been proposed to perform additional sensitivity inversions (e.g. Bergamaschi et al., 2010, 2015). To this end, we set up a series of sensitivity inversions that vary different aspects of the inversion (transport simulations, inversion algorithm, uncertainty covariance design, prior emissions, observation selection, seasonality of emissions). An overview of these sensitivity inversions is given in Table 2 and details are described in the following.

2.5.1 Transport simulation

One important source of uncertainty when using observational data from elevated sites is the potential mismatch between model and real topography. The choice of the particle release height in the model can considerably change the model's performance and may lead to systematic biases in simulated concentrations. Therefore, we quantified the effect of the release height by using a "low" and "high" release case for each of the sensitivity inversions in Table 2. One is always using the lower release heights for the CarboCount-CH stations as introduced in Sect. 2.2, whereas the other uses the higher release heights. The release heights of the more remote sites JFJ and SSL were not varied because of their less direct influence on the Swiss emissions. In addition to the release height, two different versions of the atmospheric transport model were used. The base inversion was based on FLEXPART-COSMO and a sensitivity run used the results of FLEXPART-ECMWF (S-EC).

2.5.2 Seasonal variability

In the base inversion emissions were assumed to be constant in time. However, considerable seasonal variability of the emissions especially from the agricultural sector can be expected. To test the implication of this assumption, a sensitivity run extending the state vector to separately hold emissions for each season (S-V) was set up following the common definition of winter spanning the months December, January and February (DJF) and so forth (spring: MAM, summer: JJA, fall: SON). The prior emissions and their uncertainty were set identical for all seasons. The correlation length scale between different emission times was set to $\tau_t = 90$ days (see equation 11). Reducing this time constant to 45 days had only a minor influence on the inverse emission estimate.

2.5.3 Inversion algorithm

An additional sensitivity test, replacing the Bayesian method by an extended Kalman Filter (extKF) inversion as described in Brunner et al. (2012), was conducted (case S-K). Similar to the Bayesian inversion a prior state vector is used by the extKF. In contrast to the Bayesian approach, the extKF assimilates the observations sequentially from time step to time step. In the extKF approach one baseline value and its tendency for each site are part of the state vector. In each step observations from different sites but not from different times are incorporated. This allows for a more flexible temporal evolution of the emissions and the baseline values as for the Bayesian approach. Another important difference is that the extKF method of Brunner et al. (2012) estimates the logarithm of the emissions rather than the emissions themselves to enforce positive fluxes. This renders the problem non-linear and requires the use of an extended Kalman Filter. As in the Bayesian inversion the extKF describes the uncertainties of the prior state and the model-observation uncertainty through the respective uncertainty covariance matrices **B** and **R**. In addition to these, the extKF requires an uncertainty covariance matrix **Q** that describes the uncertainty with which the state vector can change from one time step to the next.

Accordingly, uncertainties of the state vector are allowed to grow from one time step to the next, which introduces an additional amount of prior uncertainty as compared to the Bayesian approach. The matrices **B** and **R** were parameterised according to equations (9) and (12), respectively. The chosen parameter values are listed in Tab. 3. The forecast uncertainty matrix **Q** was also parameterised according to equation (9), notably with the same spatial correlation length. The diagonal elements of **Q** were set to a relative forecast uncertainty of the emissions of 0.6 % per 24 hours, which resulted in fairly constant posterior emissions in time with only a small seasonal cycle.

2.5.4 Covariance parameters

The next set of sensitivity inversions was designed to analyse the effect of different uncertainty covariance matrices. Our base inversion is based on the prior emission uncertainty as estimated by the SGHGI, which we consider to be the best knowledge of bottom-up uncertainty in Switzerland. Since Hiller et al. (2014a) used the same by-category emissions as the SGHGI to spatially disaggregate total emissions for the MAIOLICA inventory (our prior), we extrapolated the SGHGI uncertainty information to the whole inversion domain. Next to the base inversion a set of uncertainty covariance parameters as estimated by the method of maximum likelihood (ML, Michalak et al., 2005) were used (S-ML). We estimated the covariance parameters (L, f_E, τ_b, and individually for each site f_b, σ_min, σ_srr) by minimising the negative logarithm of the likelihood estimator (Michalak et al., 2005)

$$L_\theta = \frac{1}{2}\ln\left|\mathbf{MBM}^T + \mathbf{R}\right| + \frac{1}{2}\left(\boldsymbol{\chi}_\mathrm{o} - \mathbf{M}x_\mathrm{b}\right)^T\left(\mathbf{MBM}^T + \mathbf{R}\right)^{-1}\left(\boldsymbol{\chi}_\mathrm{o} - \mathbf{M}x_\mathrm{b}\right). \quad (14)$$

As a consequence of the ML optimisation posterior model residuals and posterior emission differences should follow a χ^2 distribution. To find the minimum of L_θ a multivariate optimisation routine was used. We applied the Broyden, Fletcher, Goldfarb and Shanno (BFGS) algorithm that is widely used for optimisation problems (see for example Nocedal and Wright, 2006). Initial parameter values were set equal to those used in the base inversion, but giving all sites the same σ_min of 20 nmol mol^{-1} and σ_srr of 1. To assess the ro-

bustness of the ML optimisation results an alternative algorithm was tested (Nelder–Mead), yielding very similar parameter sets.

Another sensitivity run varied the design of the model/observation uncertainty covariance by estimating the diagonal elements of the matrix from the prior RMSE at each site $\sigma_{\text{min}} = \text{RMSE}(\chi_{\text{b}} - \chi_{\text{o}})$ and applying a correction for extreme residual values according to Stohl et al. (2009) (S-S). Such extreme residuals only occurred for two observations at LHW, so that essentially a constant model uncertainty was used for each site. The off-diagonal elements were calculated in the same way as in the base inversion. For the extKF inversion it was only possible to use a fixed set of parameters σ_{min} and σ_{srr} for all sites, because by-site treatment was not yet implemented in the current version of the code. They were selected to be close to the average values used in the reference inversion. All covariance parameters used in the base, these two alternative and also the extKF inversion are compared in Table 3. In case of the Bayesian inversions, the covariance parameters differed between the two release heights with the high release showing larger values of σ_{min} for the sites BEO and LHW and all applied estimation techniques.

2.5.5 Prior emissions

The sensitivity of the inversion result to the prior emissions was tested by using different prior inventories. In a sensitivity inversion we replaced the MAIOLCIA emissions within Switzerland with those given by TNO/MACC-2 (S-T). A third sensitivity run was set up using the EDGAR (v4.2 FT2000) inventory for the base year 2010 (JRC/PBL, 2009) (S-E). In all three cases the prior uncertainty was set so that a value of $\sigma_E = 16\,\%$ was reached for the Swiss emissions, which is the uncertainty given for the SGHGI (FOEN, 2015). For individual grid cells the resulting proportionality factor was $f_{\text{E}} \approx 30\,\%$. However, the off-diagonal elements in $\mathbf{B}^E$ contributed considerably to the total country uncertainty since they were especially large for small grid cells (see Fig. S2 in the Supplement).

2.5.6 Selection of observations

Another series of sensitivity inversions was set up using different parts of the observational data (runs S-01 to S-05, Table 2). The number and combination of sites used in each inversion was varied from using individual sites to using all six sites. For each of these sensitivity cases the inversion grid was adjusted according to the total source sensitivity of the selected sites, thereby assuring that small grid cells only occurred in areas with large sensitivities. In the base inversion the two CarboCount-CH sites BEO and LHW and the two more remote sites JFJ and SSL were used, whereas the observations of FRU and GIM served for validation only.

2.5.7 Baseline treatment

As described above, the baseline mole fractions were treated as a linear interpolation between mole fractions at designated baseline nodes, the latter being optimised as part of the state vector in the inversion. The treatment of the baseline in this regional scale inversion is critical and may introduce attribution errors in the posterior emissions. Therefore, we explored two alternative methods that address certain shortcomings of our main approach. For example, there were times when the simulated smooth baseline was not able to follow apparent fast changes in the observed baseline signal. This was the case when the general advection direction towards Switzerland quickly changed from west to east, with mole fractions often being considerably elevated during easterly advection. At such transition times using the smooth baseline may lead to attribution errors in the emission field. Instead of a smooth baseline it would have been desirable to take the baseline directly from an unbiased state of a global scale model, sampling the mole fractions at the FLEXPART particle end points. However, such model output was not available for the investigation period at the time of the analysis.

The first alternative method (S-B1) was based on two baseline estimations – one for the eastern and one for the western part of the inversion domain – which were combined using a weighted mean depending on the end points of the model particles (here 4 days

before arrival at the site). Since the initial location of the particles were available for every 3 h interval, this approach allows for more flexible variations of the simulated baseline signal. As in the standard baseline treatment, prior baseline mole fractions were taken from the REBS baseline at JFJ, applied here to both the eastern and western baselines. The second alternative baseline method (S-B2) extended the approach to a three-dimensional grid of baseline mole fractions accounting not only for east–west but also for north–south and vertical gradients. Again, the initial positions of the model particles within the grid as obtained from each FLEXPART simulation were used to determine the baseline concentration at the site as a weighted average. Different from methods B and S-B1, however, only one common set of gridded baseline mole fractions was estimated and applied to all sites. Only a very coarse ($3 \times 3 \times 2$) grid, covering the inversion domain, with a 15-daily temporal resolution was used in order to limit the size of the state vector. In the vertical, the grid was separated between heights 3000 m below and above ground level. The latter was chosen to ensure that average initial sensitivities were similar for both vertical layers. Prior baseline values in the upper vertical layer were again taken from the REBS baseline at JFJ, whereas the lower layer was initialised with the REBS baseline at BEO. This ensures a negative vertical gradient in CH_4 baseline mole fractions, since estimates for BEO were generally larger than those for JFJ.

3 Results

In the following the results of the emission inversions are presented, first in a more detailed fashion for the base inversion and second in a less exhaustive way for the sensitivity inversions highlighting the differences from the base case. Note that the base inversion does not necessarily represent the best inversion set-up and most likely or best estimate of the posterior emissions. Rather, it is used as a starting point to analyse the sensitivity to different inversion settings. Although there might be a best inversion set-up in the sense that its results are closest to the truth, this best set-up is not known (as little as the true emissions are known). The ML method applied as an alternative is an objective method to tune the

free parameters of an inversion, but this does not necessarily correspond to the best set-up since it cannot account for potential biases arising from transport errors or the problem in representing the release height of the particles.

3.1 Base inversion

Average source sensitivities as calculated with FLEXPART-COSMO on the reduced grid are shown in Fig. 1 for the base inversion as the combined sensitivity of the four sites BEO, LHW, SSL, and JFJ. Source sensitivities were largest close to the sites and in general for the Swiss Plateau (see Oney et al. (2015) for a detailed discussion of source sensitivities of the CarboCount-CH sites). The pronounced south-west to north-east orientation of the maximal source sensitivities is a result of the flow channelling between the Alps and the Jura mountains (Furger, 1990). South of the Alps and outside Switzerland source sensitivities quickly declined with generally larger values for westerly compared with easterly directions. Source sensitivities towards the south-east were especially small, reflecting the shielding effect of the Alps.

In Switzerland prior emissions amounted to 178 $\mathrm{Gg\,yr^{-1}}$. After mapping the high resolution emission data to the reduced inversion grid (Fig. 2a) and applying Eq. (8), Swiss prior emissions were quantified at 183 $\mathrm{Gg\,yr^{-1}}$. The difference of 2 % can be explained by mapping artefacts along the Swiss border where inversion grid cells overlap with neighbouring countries, wrongly attributing some emissions from these to the Swiss total. The distribution of the prior emissions (Fig. 2a) in Switzerland clearly emphasises the dominating role of emissions from the agricultural sector. Emission maxima are located in the Canton of Lucerne in close vicinity to BEO and in the north-eastern part of the country towards Lake Constance in the Cantons of Thurgau and Saint Gallen. All these areas are characterised by intensive agriculture with a focus on cattle farming. Emissions from the urban centres of Zurich, Basel, Bern and Geneva, in contrast, are not especially pronounced in the MAIOLICA inventory. Within the high Alpine area, and to a smaller degree within the Jura mountains, MAIOLICA emissions are significantly smaller, but are large again in the north Italian Po Valley and also in south-western Germany.

Simulated CH_4 time series for the sites used in the base inversion with low model release heights (B low) are compared with the observations in Fig. 3. Most of the time the prior simulations were closely following the observed variability, underlining the very good performance of the transport model. However, during some periods the prior simulations considerably underestimated the observed mole fractions. This was especially true for the BEO and LHW sites and a period in March/April as well as during episodes in October and November 2013. Some of the observed temporal variability was common for all sites suggesting an important influence from large-scale weather systems, whereas at other times the signals from different sites were little correlated. The two sites on the Swiss Plateau showed the most common behaviour, while, as expected, the high altitude observations at JFJ were most decoupled from the other observations. Also as expected, peak mole fractions were larger for the sites closer to the emissions (BEO, LHW) and smaller for the higher altitude sites (SSL and especially JFJ). The transport model captured this general tendency very well. Except for JFJ, prior baseline mole fractions (based on the JFJ REBS estimate) were smaller than most observed mole fractions.

The model's skill considerably improved for the posterior simulations showing greater correlations and lower biases. The simulations more closely followed the observed variability and the bias was reduced (Fig. 3). Partly, this was achieved through changes in the baseline mole fractions. Posterior baselines were generally greater than the prior at the BEO, LHW and SSL sites, whereas they were lower than the prior at JFJ. Largest baseline increases occurred during extended periods of elevated CH_4 (e.g. March 2013). These periods were characterised by easterly advection on the south-easterly side of high pressure systems with centres over north-western to central Europe. In these situations the limited model domain and the relatively short backward integration time of four days were likely insufficient to capture all recent emission accumulation above the baseline. As a consequence, the inversion adjusted the baseline upward.

The quality of the simulated time series is summarised in Fig. 4 where coefficients of determination, R^2, are given for all sites, for both prior and posterior simulations and separately for the complete (Fig. 4a) and above-baseline signal (Fig. 4b). The performance in the

prior simulations ranged from $R^2 = 0.25$ for the site FRU to $R^2 = 0.5$ for the site GIM and the complete signal. The coefficients of determination for the above baseline signal were slightly lower, but showed the same ranking between the sites: largest at GIM followed by the sites SSL, LHW, BEO and JFJ and smallest for FRU. Posterior coefficients of determination considerably increased for all sites used in the inversion ($R^2 = 0.58$–0.69), slightly increased for FRU, but slightly decreased for GIM. Improvements were seen both for the complete signal as well as for the above-baseline signal. The ranking between the sites remained similar after the inversion.

An overall quality indicator, which not only accounts for the correlation but also for a correct representation of the amplitude of the variability, is the Taylor skill score (Taylor, 2001)

$$S = \frac{4(1+R)}{\left(\sigma_f + \sigma_f^{-1}\right)^2 (1+R_0)}, \tag{15}$$

where R is the Pearson correlation coefficient, R_0 the maximal attainable Pearson correlation of a "perfect" simulation, which is still limited by factors such as observation and representativeness uncertainty and was set to 0.9. $\sigma_f = {}^{\sigma_m}/_{\sigma_o}$ is the simulated standard deviation normalised by the observed standard deviation. S takes the value of 1 for a perfect simulation, but would take a value of 0.65 for perfectly correlated simulations that under/overestimate the observed variability by a factor of 2. The prior value of σ_f was well below 1 for all sites (0.43 to 0.71), indicating generally under-predicted peak heights, but increased in the posterior simulation to values between 0.65 to 0.8, except for GIM where it remained at 0.44. Posterior values of S for all sensitivity inversions and all sites are given in Table 4. For the base inversion S ranged from 0.78 to 0.91 for the sites used in the inversion and was smaller for the sites FRU and GIM (0.77 and 0.50). Note however, that for the latter two sites the baseline was not adjusted by the inversion, which may explain part of the weaker posterior performance. In the case of GIM it is remarkable that the correlation was comparatively large but the normalised standard deviation was very small. This may indicate that the general transport to the site was well captured by the model (correlation),

but that either local boundary layer heights or local emissions were overestimated or underestimated, respectively, so that the model was not able to simulate the observed amplitudes correctly. Taylor skill scores were very similar for posterior simulations of the base inversion using the high particle releases (B high in Table 4). Also, the prior simulation's performance was similar for low and high release heights, with lower release heights usually performing slightly better in terms of amplitude of the simulated variability and higher release heights showing slightly improved correlations. No clear preference for the lower or higher release height could be deduced from these results.

As an additional validation parameter the root mean square error (RMSE) and its reduction from prior to posterior simulations are shown in Fig. 4c and d. For sites used in the inversion the prior RMSE was between 20 and 40 $\mathrm{nmol\,mol^{-1}}$ and decreased by 15 to 25 % in the posterior simulations. For the near-surface sites FRU and GIM the RMSE did not significantly decrease after the inversion. At both sites simulated mole fractions were smaller than observed, especially at GIM. Even when using only afternoon values and when filtering for wind conditions with possibly large local influences (as done here), the transport model was not able to reproduce the amplitude of the observed variability at these sites. A reason for this poor model performance in FRU is most likely the inlet height very close to the surface and the associated high sensitivity to local emissions that cannot be captured at the resolution of the transport model. In GIM local emissions or mismatches in the local boundary layer height seem to be the main problem since the timing of the temporal variability was captured very well. The effect of including the sites GIM and FRU in the inversion is further discussed in Sect. 3.7.

We used observations from sites in more complex terrain and closer to emission sources than used in other regional scale inversion studies of CH_4 surface fluxes for the European and East Asian domain (Bergamaschi et al., 2015; Manning et al., 2011; Thompson et al., 2015). This should result in more complex variability at the sites. Nevertheless, our model performance parameters are well within the range reported previously by the above studies.

The posterior CH_4 emissions and their differences from the prior emissions are shown in Fig. 2b–d. The largest, though still modest, absolute changes (Fig. 2c) were estimated

for the region south-west of BEO. In this region with large prior emissions from agriculture, reductions were in the order of 25 %. Further reductions were estimated east of the site LHW in the canton of Thurgau (please refer to Fig. S1 for a map of the Swiss cantons) and in large parts of western Switzerland. In contrast, larger than prior emissions were obtained for north-eastern Switzerland in the Cantons of Saint Gallen and Appenzell and also beyond the border in south-western Bavaria. Emissions in northern Italy were increased but due to the weak sensitivity for this region these posterior results are subject to larger uncertainties than those on the Swiss Plateau. Relative emission increases (Fig. 2d) of up to 30 % were detected for the Appenzell region and the bordering Vorarlberg region in Austria. On the contrary, relative emission reductions appeared for the southern Black Forest. Similar patterns emerged for the base inversion when using the high release heights (see Fig. S3 in the Supplement), but posterior emissions were generally larger in this case.

In this base inversion Swiss total emissions were estimated at $179 \pm 7\,\mathrm{Gg\,yr^{-1}}$ (1σ) and $195.0 \pm 7.3\,\mathrm{Gg\,yr^{-1}}$ for the low and high particle release heights, respectively. Both values are not significantly (two-sided Welch t test) different from their prior value, indicating a high level of consistency between the bottom-up estimate of the MAIOLICA inventory and our top-down estimate. Furthermore, analytical uncertainties of the posterior were considerably reduced by about 75 %. However, the difference $\pm 15\,\mathrm{Gg\,yr^{-1}}$ in total Swiss emissions resulting from the choice of the particle release height suggests a relatively large additional contribution to the overall uncertainty due to the inversion set-up, which is not included in the analytical uncertainty.

Next to an improved reproduction of the measurement time series, the reduction of uncertainty in the emission field provides information on the quality of the inversion. Uncertainty reductions were largest close to the observation sites (Fig. 5). For the sites with larger surface sensitivities (LHW and BEO), uncertainty reductions in their vicinity were larger than for the more remote sites (SSL and JFJ). It is interesting to note that uncertainty reductions were largest in the area around and west of BEO, where also emission reductions were the largest. Uncertainty reductions were smaller for the area east of LHW, where also considerable emission reductions were established. For north-eastern Switzerland, where the

inversion produced large emission increases, uncertainty reductions were relatively small. The associated emission increases are thus less well constrained, which in turn may indicate temporally variable emissions or increased transport uncertainties for the associated flow direction.

3.2 Seasonal cycle

When allowing seasonal variability of the emission fluxes (S-V), distinct differences between the seasons are visible, although no seasonal variability was included in the prior (Figs. 6 and S4 in the Supplement). Winter-time posterior emissions were strongly reduced especially in agricultural areas. Posterior emissions during the other seasons tended to be slightly larger than their prior values.

Also the estimated emission patterns changed from season to season. In spring and summer increased posterior emissions were estimated for eastern Switzerland, the Canton of Lucerne (around BEO) and generally the pre-alpine area, whereas there was a tendency for smaller than prior emissions in western Switzerland. The strong increase around the station FRU (not used in the inversion) is consistent with the observation that the posterior model performance for the site FRU was considerably enhanced compared to the prior simulation. Performance was also enhanced compared to the posterior simulation of the base inversion both in terms of correlation and RMSE reduction, although Taylor skill scores were similar in both inversions (see Table 4). On the contrary, during fall higher than prior emissions were present in north-western and eastern Switzerland, and for small areas south of BEO and east of LHW posterior emissions were below prior estimates.

For the low model release height, total Swiss emission rates were smallest during winter ($152.2 \pm 9.7\,\mathrm{Gg\,yr^{-1}}$) but were relatively similar and close to the prior estimates during the other seasons (206.5 ± 12, 182.1 ± 13, and $202.7 \pm 11\,\mathrm{Gg\,yr^{-1}}$ for spring, summer and autumn, respectively). The annual total Swiss emissions for S-V were $185.9 \pm 6.5\,\mathrm{Gg\,yr^{-1}}$, very close to those of the base inversion. Winter-time emission rates were 18 % smaller than the annual mean. For the high model release heights, a similar but less pronounced annual

cycle was derived, which featured total annual emissions of 197 ± 7 Gg yr^{-1} and winter-time emission rates of 171 ± 10 Gg yr^{-1} (13 % lower than annual mean).

3.3 Extended Kalman Filter inversion

The extended Kalman filter inversion using low particle release heights (S-K low) yielded similar annual mean posterior emissions as the base inversion (Figs. 7 and S5 in the Supplement). Several features of the posterior emission differences obtained by the base inversion are also visible in the extKF inversion: reductions west of BEO, increases in north-eastern Switzerland, small changes in the Alpine area, small increase in the region close to GIM (shifted south-westerly as compared to base inversion). No emission reductions were, however, deduced for the area east of LHW. Overall the posterior model performance using the extKF inversion was superior (S between 0.84 and 0.95) compared to the base inversion (Table 4), which is most likely related to the time variable posterior emission field and to a smaller degree to the different treatment of baseline mole fractions.

Total Swiss emissions were estimated at 193 ± 13 and 217 ± 14 Gg yr^{-1} by the extKF inversion for the low and high particle release height, respectively. These values are considerably larger (8 and 15 %) than those of the base inversion but fall well within the range of values reported by the other sensitivity inversions using the Bayesian approach. The difference in total emissions between the low and high release case of 24 Gg yr^{-1} was considerably larger than in the base inversion (Table 4). Uncertainty estimates of the posterior emissions remained larger in the extKF case than in the base inversion, despite the fact that similar prior uncertainties and model/observation uncertainties were used in both systems. The main reason for this observation is that the uncertainties of the state vector are allowed to grow in the extKF from one time step to the next accounting for the forecast uncertainty, which introduces an additional amount of prior uncertainty.

3.4 Influence of transport model

In the sensitivity case S-EC the source sensitivities were derived from FLEXPART-ECMWF instead of FLEXPART-COSMO (see Sect. 2.2). On the one hand, FLEXPART-ECMWF may be less suitable to resolve the complex flow in the Swiss domain due to its coarser horizontal resolution. On the other hand, FLEXPART-ECMWF is a well validated model code and has been widely used for inverse modelling (e.g. Stohl et al., 2009; Thompson and Stohl, 2014; Thompson et al., 2015). Using the same inversion settings, FLEXPART-ECMWF simulations yielded generally similar posterior emissions as the base inversion (Figs. 8 and S6 in the Supplement). Common features were again the decrease west of BEO and east of LHW and the increase in north-eastern Switzerland with respect to the prior emissions. In contrast to the base inversion, large emission reductions were also assigned to most of the western part of the country towards lake Geneva. For the low release height, the model performance at the observation sites was only slightly lower compared to the base inversion as indicated by the posterior Taylor skill scores (Table 4). In contrast, posterior Taylor skill scores were slightly larger in the high release case than in the base inversion. An exception was the GIM site, for which skill scores were strongly reduced using FLEXPART-ECMWF. This may reflect the growing inability of a coarser transport model to simulate the local CH_4 contribution to the site.

Although FLEXPART-ECMWF's performance at the sites was of similar quality as for the base inversion, the uncertainty reductions of the posterior emissions (Fig. 8b) were not as pronounced in the S-EC cases (low and high) as compared to the base inversion. This can partly be attributed to the larger model uncertainty assigned in the ECMWF case (especially low particle release case) compared to the base inversion (compare Tab. 3). Total Swiss posterior emissions in the S-EC case were 171.1 ± 8.0 and $182.1 \pm 7.6\,\mathrm{Gg\,yr^{-1}}$ in the low and high particle release case, respectively, slightly smaller than in the base inversion. One possible explanation may be the coarser and, hence, potentially less dispersive behaviour of FLEXPART-ECMWF. Mesoscale flow patterns in complex terrain may contribute to effective

dispersion (Rotach et al., 2013). The coarser resolution of FLEXPART-ECMWF likely results in larger under-representation of mesoscale flow in the complex Swiss terrain.

3.5 Influence of prior emissions

Two additional spatially explicit sets of prior emissions were used to explore the effect of the prior emissions on the inversion results. The sensitivity run based on EDGAR (S-E) starts off from considerably larger prior emissions for Switzerland (228 $\mathrm{Gg\,yr^{-1}}$) and also deviates strongly in the spatial allocation of these emissions, putting more emphasis on the population centers than the MAIOLICA inventory (Hiller et al., 2014a). This can be traced back to EDGARv4.2 containing about 25 $\mathrm{Gg\,yr^{-1}}$ larger emissions from the gas distribution network (IPCC category 1B2: fugitive emissions from oil and gas; 32 vs. 8 $\mathrm{Gg\,yr^{-1}}$ in MAIOLICA), while other emission categories are similar. However, also the remaining emissions are more closely following the distribution of population density when compared with the MAIOLICA inventory, which is due to less detailed geographical information in the EDGARv4.2 inventory (Hiller et al., 2014a). Differences between the TNO inventory (S-T) and the MAIOLICA inventory are more subtle and amount to only 5 $\mathrm{Gg\,yr^{-1}}$ for the Swiss total.

In all three inversions (B, S-E and S-T) posterior emissions were very similar both in their distribution (see Figs. S3, S7, S8 in the Supplement) and also in the national total. The latter only differed by 5 $\mathrm{Gg\,yr^{-1}}$ for S-T and 10 $\mathrm{Gg\,yr^{-1}}$ for S-E despite the fact that prior emissions were 45 $\mathrm{Gg\,yr^{-1}}$ larger in the latter (Table 4). This indicates that the posterior emissions were well constrained by the observations and not solely governed by the prior emissions for which relatively small uncertainties were assigned. The strong posterior emission increase in north-eastern Switzerland was also prominent in S-E. The posterior to prior differences for S-E showed a strong emission reduction in the larger urban areas (mainly Basel, Zurich, but also Lucerne, Bern and Geneva) suggesting that the strong attribution of emissions to urban centers in the EDGAR inventory is unrealistic (Fig. 9a). In contrast to the base inversion, uncertainty reductions in the S-E case were also large for the urban areas (Fig. 9b), lending credibility to the associated emission reductions.

3.6 Influence of uncertainty covariance treatment

The inversion results using the model/observation uncertainty as estimated by the method of Stohl et al. (2009) (S-S) were smaller than in the base inversion in the low release case but differed only slightly in the high release case (see Table 4). In S-S an almost constant value (see Sect. 2.4) was given to the model/observation uncertainty of each site, while in the base inversion uncertainties tended to be larger for large above-baseline mole fractions. However, model uncertainties were mostly smaller for the base inversion except for 10 to 20 % of the observations in the "low" and less than 10 % in the "high" release case. Despite these differences in the applied model uncertainty, the distribution of posterior fluxes was similar to that of the base inversion with two exceptions: emission reductions were more pronounced in the area west of BEO and east of LHW in the S-S case and additional reduction occurred around the BEO site itself (see Fig. S9 in the Supplement). The distinct posterior increase in north-eastern Switzerland was also present in S-S.

In comparison with the base inversion, all parameters describing the uncertainty covariance matrices showed increased values when they were estimated by the maximum likelihood method (Table 3). Especially the uncertainty of the baseline, as described by parameter f_{b}, was strongly increased for all sites, but also the model uncertainties were generally larger (parameters σ_{min} and σ_{srr}). In addition, the ML method yielded an increased uncertainty of the prior emissions, resulting in a total uncertainty for Switzerland of about 30 %, indicating that the bottom-up estimate of 16 % may be too optimistic. The spatial correlation length of the prior emissions remained very close to the $L = 50\,\mathrm{km}$ used in the base inversion. The resulting posterior emissions were distributed similarly as in the base inversion. However, emission reductions were more pronounced (see Fig. S10 in the Supplement). As for the S-S sensitivity, emission reductions were also estimated for the region between BEO and LHW and only a small local increase around the BEO site remained. The total posterior emissions for Switzerland were only 158 ± 13 and $169 \pm 13\,\mathrm{Gg\,yr^{-1}}$ for the low and high particle release case, respectively. Due to the larger baseline uncertainty as estimated by the ML optimisation, adjustments of the posterior baseline were larger than in the base

inversion. As a result baseline mole fractions were raised for the sites BEO and LHW during periods of increased CH_4 observations, hence, reducing the need for increased emissions at these times and lowering the overall posterior emissions. The increased prior and model uncertainties resulted in relatively large posterior uncertainties as compared with the base inversion. The overall posterior model performance was similar to that of the base inversion. However, a larger part of the simulated variability was attributed to variations in baseline signal.

3.7 Influence of observation selection

For almost all sensitivity inversions with different subsets of observational data (S-O1 to S-O5 in Table 2) the emission reduction west of BEO could be confirmed (see Figs. S11, S12, S13, S14, S15 in the Supplement). In contrast, the reduction east of LHW was only evident in those runs that also used the observations from LHW. Similarly, the increase in north-eastern Switzerland was more pronounced if the observations from BEO were used. Relatively large emission changes were obtained at mid-range (100 to 500 km) from the sites on the Swiss Plateau when the more remote sites SSL and JFJ were not used in the inversion (S-O1 to S-O3). The larger emission changes in S-O1 to S-O3 were likely the result of attribution errors. The BEO and LHW sites were only sensitive to these more distant areas when they were also sensitive to closer emission sources. Hence, the inversion assigned increased emissions to these distant areas located behind the real emission sources. Using observations from additional sites with a different sensitivity pattern can solve this problem as it did in our base inversion, where the elevated sites JFJ and SSL with distinctly different sensitivity patterns were included.

Swiss CH_4 emissions for this set of sensitivity inversions were larger than in the base inversion (Table 4). Largest emissions ($214.3 \pm 11\,\mathrm{Gg\,yr^{-1}}$ in the low release case) were obtained when only the site LHW was used (S-O2), resulting in large emission increases in western Switzerland, whereas posterior emissions remained similar to the base inversion close to the BEO and LHW sites. This pattern is most likely due to the problem of shadowing effects.

S-O5, the inversion using all six sites, resulted in comparatively large total emissions for Switzerland as well (208.8 ± 6 Gg yr^{-1} in the low release case). Emissions were largely increased around the site GIM and further west as a result of the large mole fractions observed at GIM. As discussed earlier, it seems likely that large local emissions around GIM could not properly be accounted for by the inversion system and were spread out over a larger area, resulting in overall larger national emissions.

It is interesting to note that including the additional observations from GIM and FRU only slightly reduced the overall uncertainty of the national emission estimate in comparison to the base inversion (from 7.0 to 6.0 Gg yr^{-1} for the low release case). In contrast, using the two sites LHW and BEO in combination instead of either one of them individually, reduced the uncertainty from about 11 to 7.9 Gg yr^{-1}. Hence, the additional gain in terms of uncertainty reduction was relatively small when adding the sites GIM and FRU. which would have been expected from their more localised sensitivity as compared to the other sites.

Of the sensitivity inversions with differing observation data the results of the case using only observations from BEO (S-O1) was closest to those of the base inversion, both in terms of total emissions and of geographic distribution. This supports the expectation that a tall tower site should be best suited for inverse modelling (as can also be seen by the dominating role of BEO in the uncertainty reduction; Fig. 5). However, the estimation of other Swiss GHG fluxes using observations from this site alone will strongly depend on our ability to correctly assign baseline values and the question if shadowing effects can be neglected.

3.8 Influence of baseline treatment

As mentioned above, the treatment of baseline mole fractions is critical in order to avoid attribution errors in the emission field. When varying the prior baseline uncertainty in our base inversion, considerable changes in posterior emissions indicated this sensitivity. Doubling (halving) the prior baseline uncertainty results in -19 Gg yr^{-1} (+31 Gg yr^{-1}) total Swiss emissions as compared to the base inversion (low particle release height). In both cases the obtained posterior baselines did not seem very reasonable (too smooth, too closely following

the observed short term variability), so that these cases can be seen as the extreme range of the baseline influence. Nevertheless, by exploring different baseline treatments, the sensitivity to baseline assumptions was further documented. Comparing the inversion results of the two inversions with alternative baseline treatment (S-B1 and S-B2; see Sect. 2.5 for details) with the base inversion did not reveal any large differences in terms of geographical distribution (see Figs. S16 and S17 in the Supplement). In the case of S-B2 the reductions in the western part of Switzerland were confined to the area between GIM and BEO and also the reductions north of BEO (as seen in the base inversion) were turned into increases. Especially S-B2 yielded enhanced model performance that was mainly due to a more detailed description of the temporal variability of the baseline (Table 4). Total Swiss emissions for S-B1 remained very similar to the base inversion but were considerably larger for S-B2 (195.1 ± 6.9 and $223.6 \pm 6.9\,\mathrm{Gg\,yr^{-1}}$ for low and high particle release height, respectively). In S-B2, where a coarse three-dimensional grid of baseline mole fractions was optimised, their posterior values were largest for the eastern and low grid cells and during the previously highlighted period in March 2013 and again in the winter 2013/14. Furthermore, vertical gradients were smaller during the summer months than during the winter (see Fig. S18 in the Supplement). This general distribution is in line with our expectations (higher mole fractions towards surface and more continental areas) and lends credibility to this kind of baseline estimation. One further advantage of analysing a common baseline grid for all sites is its possible use for the validation sites as well. Indeed, a larger improvement in posterior performance at the sites FRU and GIM can be seen for S-B2 than in any other sensitivity inversion in which the sites were used for validation only.

4 Discussion

4.1 National total emissions

The main result of the present study is summarised in Fig. 10 in terms of a histogram of total Swiss CH_4 emissions for the investigation period March 2013 to February 2014 taken

from all sensitivity inversions. The estimates from the individual sensitivity inversions almost follow a normal distribution. A clear average difference between sensitivity runs using the high and low particle release heights of 20 $Gg\,yr^{-1}$ is apparent. This difference is larger than the one between the results taken from the two employed transport models FLEXPART-ECMWF and FLEXPART-COSMO (12 $Gg\,yr^{-1}$, 5 %). The latter supports the large degree of consistency between the two transport models and the underlying meteorology. In an inverse estimate of HFC-134a emissions from the continental USA, Hu et al. (2015) had observed a somewhat larger emission difference (20 %) when using source sensitivities obtained from two different dispersion models (HYSPLIT-NAM12, STILT-WRF) with similar horizontal resolution.

To derive an average national emission over all sensitivity inversions, we assigned the same weight to each sensitivity run and calculated a straightforward mean over all sensitivity inversions. This is a rather pragmatic approach, since some sensitivity inversions using, for example, only one site cannot be expected to be equally good as the base inversion with four sites. However, we are lacking a more objective measure that would allow us to assign quantitative weights to the different runs. Our estimates can be compared to the bottom-up estimates that the Swiss Federal Office for the Environment reported to the UNFCCC in the years 2014 and 2015 (Table 5). Please note that Swiss emissions are reported annually for the reporting period 1990 to two years before the submission date. Methodological updates from one year to another usually influence the whole reporting period (FOEN, 2014, 2015). We refer here to the emissions reported for the year 2012, since estimates for this year are available from the 2014 and 2015 reporting. According to the 2015 reporting, emission changes from 2012 to 2013 were small ($-0.14\,Gg\,yr^{-1}$) (FOEN, 2015). The estimate of CH_4 emissions submitted to the UNFCCC in 2014 for the year 2012 was $176 \pm 28\,Gg\,yr^{-1}$. Our prior was based on these estimates plus a small contribution from natural emissions of 3 $Gg\,yr^{-1}$. Our posterior estimates were slightly but not significantly larger. This is true for the mean obtained from the two base inversions ($187 \pm 10\,Gg\,yr^{-1}$) as well as for the mean over all sensitivity inversions ($196 \pm 18\,Gg\,yr^{-1}$). The latter value should be seen as our best estimate of the Swiss CH_4 emissions. It is closer to the bottom-up estimate of

$206 \pm 33\,\mathrm{Gg\,yr^{-1}}$ reported in 2015 (FOEN, 2015) as to the one reported previously. The differences in the reporting are due to updated emission factors and methodologies in the national inventory. Our inversion results support these updates.

Our overall uncertainty estimate is based on the standard deviation of all sensitivity inversions and is considerably larger than any of the uncertainty estimates of the individual inversions (Table 4). Despite this fact, the overall posterior uncertainty remains smaller than the prior uncertainty. One possible reason for the relatively small posterior uncertainty of individual inversions may be seen in the small prior uncertainty of 16 % for the national total. Similarly, when applying the ML method, considerably larger prior uncertainties in the range of 30 % were suggested (see Sect. 3.6). However, posterior uncertainties of the ML sensitivity runs (S-ML in Table 4) were still considerably smaller than our overall uncertainty. Another reason for small posterior uncertainties could be an underestimated model/observation uncertainty, lending too much trust to the simulation of the observations and in turn reducing posterior uncertainties. However, model/observation uncertainties were optimised in the same step as prior uncertainties with the ML method and were not estimated to be considerably different from the base set-up (see Table 3). These considerations lead to the conclusion that the enhanced posterior uncertainty over all sensitivity runs needs to be seen as the contribution of systematic uncertainties that are introduced by the specific set-up of the inversion system and cannot be fully covered by the analytical estimate of the Bayesian analysis, a result that has also been obtained in previous inversion studies (e.g., Bergamaschi et al., 2010, 2015; Ganesan et al., 2014).

4.2 Spatio-temporal emission patterns

Considerable emission differences were observed between the seasons, with winter-time emissions being 13 to 18 % lower than the annual average. Since the largest winter-time reduction was deduced for areas with large cattle density, it seems very likely that the estimated reductions are connected with the agricultural sector. This observation was also true for the north-eastern part of Switzerland where, although annual emissions were increased, these increases were largest in spring and summer (see Fig. 6). When compared

to the prior emissions from the agricultural sector only (150 $Gg\,yr^{-1}$, FOEN, 2014), the estimated seasonal posterior variability would be around 22 %. The latter is well in line with Gao et al. (2011) who estimated the seasonal variability of CH_4 emissions from a dairy cow farmstead in northern China. A major contribution to the annual variability may stem from CH_4 emissions from manure handling and storage, which strongly depends on temperature. Zeitz et al. (2012) speculated that Swiss CH_4 emissions from manure handling should be lower than estimated by FOEN (2014), since their observed emission factors were significantly smaller than those suggested by IPCC and used by FOEN (2014). However, their results were based on laboratory experiments that yet need to be validated in the field. Furthermore, Zeitz et al. (2012) suggest that emissions from manure handling should be significantly reduced or even cease during winter, considering the average temperatures in Switzerland. Accounting for the temperature of the manure storage, which may be well above the ambient temperature, in the emission calculation, a 50 % wintertime reduction was estimated in the bottom-up inventory (FOEN, 2015). Furthermore, seasonal variability in emissions from ruminants may be induced by seasonal variability of productivity, especially of dairy cows. In Switzerland it is common practice to time the calving date in the spring so that the cows reach their largest productivity at the point of largest feed availability (spring/summer). Since productivity and CH_4 emissions are roughly proportional, direct ruminant emissions should also follow a seasonal cycle with a minimum in the winter months (FOEN, 2015). The temporal variability in our inversion results largely agrees with these considerations and, hence, fits well to our understanding of the main agricultural emission processes in Switzerland. Furthermore, we had seen that mean annual posterior emissions were about 10 to 20 % lower in agricultural areas in our base inversion (B low). Taking the mean over all sensitivity inversions this reduction is around 5 to 15 % as compared to the prior, which was based on the 2014 reporting. Considering the larger emissions from agriculture in the 2015 reporting, our mean posterior emissions in agricultural areas suggest that the revised bottom-up inventory (FOEN, 2015) overestimates agricultural emissions by 10 to 20 %. From the inferred seasonality we conclude that this is most likely because emissions from manure handling are overestimated. Our findings are in line with recent in-

version results (covering the period 2009 to 2011) for Europe that indicate similar to lower emissions as compared to EDGAR (Alexe et al., 2015; Turner et al., 2015; Ganesan et al., 2015), whereas for the USA a number of studies suggest a significant underestimation of ruminant emissions in the EDGAR-v4.2 and USA EPA inventories (Miller et al., 2013; Wecht et al., 2014; Turner et al., 2015).

Our posterior results depend little on the prior emission distribution (B vs. S-E and S-T) and corrected the large emissions in urban areas given by the EDGARv4.2 inventory downwards. Hence, we conclude that the emissions from natural gas distribution and use in the SGHGI/MAIOLICA inventory is more realistic than in EDGARv4.2. The SGHGI emissions from natural gas distribution of 8 $\mathrm{Gg\,yr^{-1}}$ correspond to < 0.4 % of the Swiss natural gas consumption (FOEN, 2015). This is in contrast to recent studies from the USA where a large underestimation of fugitive emissions was established in the inventories for different metropolitan areas (Wennberg et al., 2012; McKain et al., 2015) and fractional loss rates between 2.5 and 6 % were established. However, these results may not be representative for the USA as a whole. According to the SGHGI, fugitive emissions were reduced in Switzerland by 36 % since 1990 mainly due to a gradual replacement of cast-iron pipes by polyethylene pipes (FOEN, 2015). Our results support the reductions documented in the SGHGI and, thus, the success of this emission reduction measure. This also highlights that large reduction potentials can be expected for other countries as well when modernisation of the infrastructure is promoted.

CH_4 emissions from composting and anaerobic digestion (IPCC 5B), mainly in the conversion of biogenic waste to biogas in small scale facilities, were amended from 5 to 16 $\mathrm{Gg\,yr^{-1}}$ from the 2014 to the 2015 reporting (Table 5). In our prior inventory, these emissions were not explicitly localised (Hiller et al., 2014a). Since our prior was based on the earlier 5 $\mathrm{Gg\,yr^{-1}}$ estimate, an increase in regions with intensive biogas production should have been detectable. However, the biogas and composting plants are approximately evenly distributed across the Swiss Plateau in areas of dominating agricultural use. Hence, it is impossible to finally attribute any of the observed posterior emission differences to this emission process. Similarly and as already indicated by Hiller et al. (2014a), emissions from

waste water treatment were probably underestimated in previous FOEN estimates. In the most recent reporting from 2015, these emissions were 6.77 $Gg\,yr^{-1}$, which is an increase by a factor of 15 compared to previous reports. The spatial distribution of CH_4 emissions from waste water treatments should mainly follow the population density. Although, our inversion results do not support increased emissions in densely populated areas, the relatively small emission revision (compared to the total emissions) may be very difficult to detect.

4.3 Unidentified source in north-eastern Switzerland

The largest emission changes that were localised by the inversion and were present in almost all sensitivity inversions were those in the north-eastern part of Switzerland in the Cantons of Saint Gallen and Appenzell. These areas are also dominated by agriculture and the estimated increase, hence, contradicts the reductions in other agricultural regions. The area contributed about 16.3 % to the national emissions in our prior inventory. This contribution was increased to 22.5 % in the posterior estimate of the base inversion, an increase of 6.2 $Gg\,yr^{-1}$. One possible reason for the increase could be systematic biases in the transport simulations and in the balance between baseline and emission adjustment. One argument against this possibility is that the increase was observed also when using FLEXPART-ECMWF instead of FLEXPART-COSMO (see Sect. 3.4) and it seems unlikely that the same systematic bias would be inherent to both meteorological inputs. Furthermore, FLEXPART-ECMWF calculations were not as restricted by the limited model domain as FLEXPART-COSMO simulations (see discussion above). However, all inversions using either one of the three different methods to adjust the baseline yielded similar increases in north-eastern Switzerland. Another possible reason for the increased emissions could be an emission source close to the observational sites that could not be described correctly by the limited model resolution and whose contributions were wrongly assigned to the respective area. Again, this seems unlikely, since the increase was present in sensitivity inversions using either one of the sites on the Swiss Plateau (S-O1, S-O2). In conclusion and although we cannot completely rule out inversion artefacts, it seems likely that the es-

timated increase represents a real emission source that is not present or under-estimated in our prior inventory.

This raises the question which processes may be responsible for the detected emissions. A possible candidate is an erroneous spatial distribution of ruminant emissions within Switzerland. However, in Switzerland the number of ruminants by animal species needs to be reported at the farm level and this information, aggregated to communities, was used for distributing agricultural emissions in the prior inventory (Hiller et al., 2014a). Different cow breeds may have different CH_4 emissions factors. The dominating breeds in Switzerland are Brown Swiss and Holstein, for which similar emissions factors have been reported (Felber et al., 2015, and references therein). Different manure management methods (e.g., Owen and Silver, 2015) and diet types (e.g., Klevenhusen et al., 2011) may also lead to variations in per head emission factors. To our knowledge, detailed investigations of emission factors under real Swiss farming conditions and their spatial variability are currently not available. The large emission factors given by (Owen and Silver, 2015) for manure storage in anaerobic lagoons do not apply to Switzerland, since this storage type does not exist here (FOEN, 2015). Therefore, effects of spatial variability of herd composition and management cannot be excluded, although it seems unlikely that these could fully explain the differences estimated by the inversion. A typical farming practice in Switzerland is moving grassing cows towards elevated Alpine pastures during the summer months. This was considered in the prior by redistributing 4 % of the national ruminant emissions to Alpine pastures (Hiller et al., 2014a). Although there are extended areas of Alpine pastures present in north-eastern Switzerland, these are not more prominent than in other Alpine areas where we did not observe increased posterior emissions. Furthermore, increased emissions in north-eastern Switzerland were also observed by the inversion for the winter and spring periods, when the Alpine pastures are unoccupied. Possible additional sources of anthropogenic CH_4 in north-eastern Switzerland may stem from biological treatment of waste in composting and anaerobic digestion facilities, solid waste disposal, waste water treatment, and natural gas distribution. Currently we have no indication that either of these processes shows a specifically high density in the given area.

This leaves the possibility of an underestimated or unaccounted natural CH_4 source. The net natural emissions accounted for by Hiller et al. (2014a) were very small ($\approx 3\,\mathrm{Gg\,yr^{-1}}$) compared to their anthropogenic counterpart ($\approx 180\,\mathrm{Gg\,yr^{-1}}$). Emissions from wetlands and lakes are thought to be the largest natural source in Switzerland ($4.6\,\mathrm{Gg\,yr^{-1}}$). Although there are a number of small wetlands and lakes situated in the Cantons of Appenzell, their fractional coverage and total area is not larger than in other areas (for example Entlebuch south-west of BEO). Furthermore, we have no indication that climate variability within the domain could have impacted the drivers of wetland emissions (precipitation, temperature) in an inhomogeneous way to explain large regional differences. Aerobic soils (forest and agricultural) are generally thought to be CH_4 sinks and were estimated to contribute a negative CH_4 flux of -4.3 to $-2.8\,\mathrm{Gg\,yr^{-1}}$ (Hiller et al., 2014a). Nevertheless, under anaerobic conditions methanogensis may dominate in deep organic soils, which can be found in wetland or peatland areas. When former peatlands are re-wetted (either due to accidental flooding or renaturation) they have been shown to become a significant CH_4 source depending on water table depth, the abundance of vascular vegetation transporting CH_4 from the root space to the atmosphere and the amount of available carbon in plant litter (Couwenberg and Hooijer, 2013). Organic soils were not considered as CH_4 sources in our prior. One large area of deep organic soils in Switzerland is located in the Alpine Rhine valley (Wüst-Galley et al., 2015), only slightly east of the area of our largest posterior increase. This possible source though remains uncertain since the area in question is used for agriculture and should be well drained throughout most of the year. The only other large area of converted peatland in Switzerland is the Seeland region around the GIM site, possibly contributing to the large CH_4 concentrations observed there (see Sects. 2.1 and 3.1). Admittedly, river re-routing and drainage systems should keep the water table low in this area. In conclusion, we cannot explicitly determine which process may have caused the increased posterior emissions in north-eastern Switzerland. Additional studies using data from more recent observations and/or additional sites will be needed to clarify these open questions.

5 Conclusions

We applied a high resolution atmospheric transport model to simulate the CH_4 observations of the CarboCount-CH network and used inversion techniques to estimate total Swiss CH_4 emissions and their geographical distribution for the period March 2013 to February 2014. A series of sensitivity inversions (varying the treatment of temporal variability of the emissions, the transport model, the inversion algorithm, the prior emissions, the uncertainty covariance matrices, the selected observations, and the baseline treatment) confirm the robustness and independent character of our results.

Our best estimate of total Swiss CH_4 emissions ($196 \pm 18\,\mathrm{Gg\,yr^{-1}}$) largely supports the bottom-up estimate as reported by the Swiss Federal Office for the Environment ($206 \pm 33\,\mathrm{Gg\,yr^{-1}}$, reported to UNFCCC in 2015 for the year 2012). The overall uncertainty as obtained from all sensitivity inversions (10 %) was larger than the analytical uncertainty of any individual sensitivity inversion, but still considerably reduced the uncertainty associated with the bottom-up estimate (16 %). Our results support the effectiveness of a well informed bottom-up inventory, calibrated to local to regional emission processes. A similar conclusion was drawn by Zavala-Araiza et al. (2015) who designed an updated bottom-up inventory for a gas production area in Texas, using locally observed emission factors. Although their bottom-up estimates were at least two times larger than conventional bottom-up estimates, they largely agreed with top-down estimates in the same area.

The inversion results indicate a redistribution of CH_4 as compared to the spatially explicit bottom-up inventory. Large winter time posterior emission reductions in regions dominated by agricultural emissions suggest that these are overestimated on an annual basis by 10 to 20 % in the most recent bottom-up inventory and that manure handling may be the responsible process. Our findings agree with recent inverse modelling of European scale CH_4 emissions that suggest similar to lower emission rates than in the EDGAR inventory. This is in contrast to recent studies from the USA that suggested considerably larger emissions from ruminants than reported in bottom-up inventories (Miller et al., 2013; Wecht et al., 2014; Turner et al., 2015). An area of increased posterior emissions in north-eastern Switzerland

could not be assigned to a single most likely source process. Emissions from previously drained peatlands may be responsible for this observation. However, this suggestion needs further investigation.

Bottom-up estimates indicate that Swiss national emissions decreased by about 20 % since the 1990s, mainly due to a reduction in livestock numbers and improvements in the gas distribution network (FOEN, 2015). The latter can be supported by our study, which did not assign large emissions to densely populated areas and strongly corrected such emissions when present in the prior estimate (EDGAR inventory). This again is in contrast to recent studies from the USA that showed, at least for two metropolitan areas, larger than expected emissions from natural gas distribution (Wennberg et al., 2012; McKain et al., 2015) and provides evidence for the efficiency of comparatively simple modernisation efforts to reach greenhouse gas reduction targets.

Our results also demonstrate the feasibility of using high-resolution transport models and continuous atmospheric observations to deduce regional scale surface fluxes with a horizontal resolution required to retrace the underlying emission/uptake processes. This conclusion is especially encouraging when considering the complex topography of the study area and for future inverse modelling studies of the two other trace gases observed within CarboCount-CH: carbon dioxide and carbon monoxide. Inversion results using data from two sites on the Swiss Plateau and two elevated sites (base inversion) were consistent with a sensitivity inversion that used only the tall tower observations of Beromünster (212 m a.g.l.). The latter emphasizes the special value of tall tower observations in deriving regional scale fluxes. Sustaining a dense observational network like CarboCount-CH will allow for independent monitoring of future climate agreements.

The Supplement related to this article is available online at doi:10.5194/acpd-0-1-2016-supplement.

Acknowledgements. This study was funded by the Swiss Federal Office for the Environment (FOEN) and by the Swiss National Science Foundation (SNSF) as part of the "CarboCount-CH" Siner-

gia Project (Grant Number: CRSII2_136273). We thank the International Foundation High Altitude Research Stations Jungfraujoch and Gornergrat (HFSJG) for the opportunity to perform experiments on the Jungfraujoch, MeteoSwiss for providing meteorological observations at the site Lägern Hochwacht and COSMO model analysis, and Swiss FLUXNET for the meteorological observations at Früebüel. Measurements at Jungfraujoch were partly performed as part of the Swiss contribution to ICOS (www.icos-infrastructure.eu). We thank the two anonymous reviewers for their constructive comments and suggestions.

References

Alexe, M., Bergamaschi, P., Segers, A., Detmers, R., Butz, A., Hasekamp, O., Guerlet, S., Parker, R., Boesch, H., Frankenberg, C., Scheepmaker, R. A., Dlugokencky, E., Sweeney, C., Wofsy, S. C., and Kort, E. A.: Inverse modelling of CH4 emissions for 2010-2011 using different satellite retrieval products from GOSAT and SCIAMACHY, Atmos. Chem. Phys., 15, 113–133, doi:10.5194/acp-15-113-2015, 2015.

Baldauf, M., Seifert, A., Förstner, J., Majewski, D., Raschendorfer, M., and Reinhardt, T.: Operational Convective-Scale Numerical Weather Prediction with the COSMO Model: description and Sensitivities, Mon. Weather Rev., 139, 3887–3905, doi:10.1175/MWR-D-10-05013.1, 2011.

Bamberger, I., Stieger, J., Buchmann, N., and Eugster, W.: Spatial variability of methane: attributing atmospheric concentrations to emissions, Environ. Pollut., 190, 65–74, doi:10.1016/j.envpol.2014.03.028, 2014.

Bamberger, I., Oney, B., Brunner, D., Henne, S., Leuenberger, M., Buchmann, N., and Eugster, W.: Observation of atmospheric methane and carbon dioxide: tall tower or mountain top stations?, Bound. Lay. Meteorol., in review, 2015.

Bergamaschi, P., Bräunlich, M., Marik, T., and Brenninkmeijer, C. A. M.: Measurements of the carbon and hydrogen isotopes of atmospheric methane at Izaña, Tenerife: seasonal cycles and synoptic-scale variations, J. Geophys. Res.-Atmos., 105, 14531–14546, doi:10.1029/1999JD901176, 2000.

Bergamaschi, P., Krol, M., Dentener, F., Vermeulen, A., Meinhardt, F., Graul, R., Ramonet, M., Peters, W., and Dlugokencky, E. J.: Inverse modelling of national and European CH_4 emissions using the atmospheric zoom model TM5, Atmos. Chem. Phys., 5, 2431–2460, doi:10.5194/acp-5-2431-2005, 2005.

Bergamaschi, P., Krol, M., Meirink, J. F., Dentener, F., Segers, A., van Aardenne, J., Monni, S., Vermeulen, A. T., Schmidt, M., Ramonet, M., Yver, C., Meinhardt, F., Nisbet, E. G., Fisher, R. E., O'Doherty, S., and Dlugokencky, E. J.: Inverse modeling of European CH4 emissions 2001–2006, J. Geophys. Res.-Atmos., 115, D22309, doi:10.1029/2010JD014180, 2010.

Bergamaschi, P., Houweling, S., Segers, A., Krol, M., Frankenberg, C., Scheepmaker, R. A., Dlugokencky, E., Wofsy, S. C., Kort, E. A., Sweeney, C., Schuck, T., Brenninkmeijer, C., Chen, H., Beck, V., and Gerbig, C.: Atmospheric CH4 in the first decade of the 21st century: inverse modeling analysis using SCIAMACHY satellite retrievals and NOAA surface measurements, J. Geophys. Res.-Atmos., 118, 7350–7369, doi:10.1002/jgrd.50480, 2013.

Bergamaschi, P., Corazza, M., Karstens, U., Athanassiadou, M., Thompson, R. L., Pison, I., Manning, A. J., Bousquet, P., Segers, A., Vermeulen, A. T., Janssens-Maenhout, G., Schmidt, M., Ramonet, M., Meinhardt, F., Aalto, T., Haszpra, L., Moncrieff, J., Popa, M. E., Lowry, D., Steinbacher, M., Jordan, A., O'Doherty, S., Piacentino, S., and Dlugokencky, E.: Top-down estimates of European CH_4 and N_2O emissions based on four different inverse models, Atmos. Chem. Phys., 15, 715–736, doi:10.5194/acp-15-715-2015, 2015.

Berhanu, T. A., Satar, E., Schanda, R., Nyfeler, P., Moret, H., Brunner, D., Oney, B., and Leuenberger, M.: Measurements of greenhouse gases at Beromünster tall tower station in Switzerland, Atmos. Meas. Tech. Discuss., 8, 10793–10822, doi:10.5194/amtd-8-10793-2015, 2015.

Brunner, D., Henne, S., Keller, C. A., Reimann, S., Vollmer, M. K., O'Doherty, S., and Maione, M.: An extended Kalman-filter for regional scale inverse emission estimation, Atmos. Chem. Phys., 12, 3455–3478, doi:10.5194/acp-12-3455-2012, 2012.

Brunner, D., Henne, S., Keller, C. A., Vollmer, M. K., and Reimann, S.: Estimating European Halocarbon Emissions Using Lagrangian Backward Transport Modeling and in Situ Measurements at the Jungfraujoch High-Alpine Site, in: Lagrangian Modeling of the Atmosphere, edited by Lin, J. C., Gerbig, C., Brunner, D., Stohl, A., Luhar, A., and Webley, P., vol. 200 of Geophysical Monographs V, 207–221, AGU, Washington, DC, 2013.

Chen, Y. H. and Prinn, R. G.: Estimation of atmospheric methane emissions between 1996 and 2001 using a three-dimensional global chemical transport model, J. Geophys. Res.-Atmos., 111, D10307, doi:10.1029/2005JD006058, 2006.

Collaud Coen, M., Praz, C., Haefele, A., Ruffieux, D., Kaufmann, P., and Calpini, B.: Determination and climatology of the planetary boundary layer height above the Swiss plateau by in situ and remote sensing measurements as well as by the COSMO-2 model, Atmos. Chem. Phys., 14, 13 205–13 221, doi:10.5194/acp-14-13205-2014, 2014.

Couwenberg, J. and Hooijer, A.: Towards robust subsidence-based soil carbon emission factors for peat soils in south-east Asia, with special reference to oil palm plantations, Mires and Peat, 12, 1–13, 2013.

Dentener, F., van Weele, M., Krol, M., Houweling, S., and van Velthoven, P.: Trends and inter-annual variability of methane emissions derived from 1979-1993 global CTM simulations, Atmos. Chem. Phys., 3, 73–88, doi:10.5194/acp-3-73-2003, 2003.

Dlugokencky, E. J., Myers, R. C., Lang, P. M., Masarie, K. A., Crotwell, A. M., Thoning, K. W., Hall, B. D., Elkins, J. W., and Steele, L. P.: Conversion of NOAA atmospheric dry air CH4 mole fractions to a gravimetrically prepared standard scale, J. Geophys. Res.-Atmos., 110, D18306, doi:10.1029/2005jd006035, 2005.

Emanuel, K. A. and Zivkovic-Rothman, M.: Development and evaluation of a convection scheme for use in climate models, J. Atmos. Sci., 56, 1766–1782, doi:10.1175/1520-0469(1999)056<1766:DAEOAC>2.0.CO;2, 1999.

Empa: Technischer Bericht zum Nationalen Beobachtungsnetz für Luftfremdstoffe (NABEL) 2015, Tech. Rep. http://www.empa.ch/web/s503/nabel, Empa, available at: http://www.empa.ch/documents/56101/246436/Nabel-technischer-bericht-15/, last access: 14 December 2015.

Enting, I. G.: Inverse Problems in Atmospheric Constituent Transport, Cambridge University Press, 2002.

Eugster, W., DelSontro, T., and Sobek, S.: Eddy covariance flux measurements confirm extreme CH_4 emissions from a Swiss hydropower reservoir and resolve their short-term variability, Biogeosciences, 8, 2815–2831, doi:10.5194/bg-8-2815-2011, 2011.

Felber, R., Münger, A., Neftel, A., and Ammann, C.: Eddy covariance methane flux measurements over a grazed pasture: effect of cows as moving point sources, Biogeosciences, 12, 3925–3940, doi:10.5194/bg-12-3925-2015, 2015.

FOEN: Switzerland's greenhouse gas inventory 1990–2012, Submission of April 2014 under the United Nations Framework Convention on Climate Change and under the Kyoto Protocol, Tech. rep., Federal Office for the Environment (FOEN), 2014.

FOEN: Switzerland's greenhouse gas inventory 1990–2013, Submission of April 2015 under the United Nations Framework Convention on Climate Change and under the Kyoto Protocol, Tech. rep., Federal Office for the Environment (FOEN), 2015.

Forster, C., Stohl, A., and Seibert, P.: Parameterization of convective transport in a Lagrangian particle dispersion model and its evaluation, J. Appl. Meteorol. Clim., 46, 403–422, doi:10.1175/JAM2470.1, 2007.

Furger, M.: Die Radiosondierungen von Payerne: dynamisch-klimatologische Untersuchungen zur Vertikalstruktur des Windfeldes, Ph. D. thesis, University of Bern, zugl. Diss., Univ. Bern, 1990, 1990.

Gal-Chen, T. and Somerville, R. C. J.: On the use of a coordinate transformation for the solution of the Navier–Stokes equations, Journal of Computational Physics, 17, 209–228, doi:10.1016/0021-9991(75)90037-6, 1975.

Ganesan, A. L., Rigby, M., Zammit-Mangion, A., Manning, A. J., Prinn, R. G., Fraser, P. J., Harth, C. M., Kim, K. R., Krummel, P. B., Li, S., Mühle, J., O'Doherty, S. J., Park, S., Salameh, P. K., Steele, L. P., and Weiss, R. F.: Characterization of uncertainties in atmospheric trace gas inversions using hierarchical Bayesian methods, Atmos. Chem. Phys., 14, 3855–3864, doi:10.5194/acp-14-3855-2014, 2014.

Ganesan, A. L., Manning, A. J., Grant, A., Young, D., Oram, D. E., Sturges, W. T., Moncrieff, J. B., and O'Doherty, S.: Quantifying methane and nitrous oxide emissions from the UK and Ireland using a national-scale monitoring network, Atmos. Chem. Phys., 15, 6393–6406, doi:10.5194/acp-15-6393-2015, 2015.

Gao, Z., Yuan, H., Ma, W., Li, J., Liu, X., and Desjardins, R. L.: Diurnal and Seasonal Patterns of Methane Emissions from a Dairy Operation in North China Plain, Advances in Meteorology, 2011, 190234, doi:10.1155/2011/190234, 2011.

Gerbig, C., Lin, J. C., Munger, J. W., and Wofsy, S. C.: What can tracer observations in the continental boundary layer tell us about surface-atmosphere fluxes?, Atmos. Chem. Phys., 6, 539–554, doi:10.5194/acp-6-539-2006, 2006.

Gerbig, C., Körner, S., and Lin, J. C.: Vertical mixing in atmospheric tracer transport models: error characterization and propagation, Atmos. Chem. Phys., 8, 591–602, doi:10.5194/acp-8-591-2008, 2008.

Hein, R., Crutzen, P. J., and Heimann, M.: An inverse modeling approach to investigate the global atmospheric methane cycle, Global Biogeochem. Cy., 11, 43–76, doi:10.1029/96GB03043, 1997.

Henne, S., Brunner, D., Folini, D., Solberg, S., Klausen, J., and Buchmann, B.: Assessment of parameters describing representativeness of air quality in-situ measurement sites, Atmos. Chem. Phys., 10, 3561–3581, doi:10.5194/acp-10-3561-2010, 2010.

Hiller, R. V., Bretscher, D., DelSontro, T., Diem, T., Eugster, W., Henneberger, R., Hobi, S., Hodson, E., Imer, D., Kreuzer, M., Künzle, T., Merbold, L., Niklaus, P. A., Rihm, B., Schellenberger, A., Schroth, M. H., Schubert, C. J., Siegrist, H., Stieger, J., Buchmann, N., and Brunner, D.: Anthro-

pogenic and natural methane fluxes in Switzerland synthesized within a spatially explicit inventory, Biogeosciences, 11, 1941–1959, doi:10.5194/bg-11-1941-2014, 2014a.

Hiller, R. V., Neininger, B., Brunner, D., Gerbig, C., Bretscher, D., Künzle, T., Buchmann, N., and Eugster, W.: Aircraft-based CH4 flux estimates for validation of emissions from an agriculturally dominated area in Switzerland, J. Geophys. Res.-Atmos., 119, 4874–4887, doi:10.1002/2013JD020918, 2014b.

Houweling, S., Kaminski, T., Dentener, F., Lelieveld, J., and Heimann, M.: Inverse modeling of methane sources and sinks using the adjoint of a global transport model, J. Geophys. Res.-Atmos., 104, 26137–26160, doi:10.1029/1999JD900428, 1999.

Hu, L., Montzka, S. A., Miller, J. B., Andrews, A. E., Lehman, S. J., Miller, B. R., Thoning, K., Sweeney, C., Chen, H., Godwin, D. S., Masarie, K., Bruhwiler, L., Fischer, M. L., Biraud, S. C., Torn, M. S., Mountain, M., Nehrkorn, T., Eluszkiewicz, J., Miller, S., Draxler, R. R., Stein, A. F., Hall, B. D., Elkins, J. W., and Tans, P. P.: U. S. emissions of HFC-134a derived for 2008–2012 from an extensive flask-air sampling network, J. Geophys. Res.-Atmos., 120, 801–825, doi:10.1002/2014JD022617, 2015.

IPCC: 2006 IPCC Guidelines for National Greenhouse Gas Inventories, available at: http://www.ipcc-nggip.iges.or.jp/public/2006gl/index.html, last access: 9 September 2015, 2006.

Jeong, S., Zhao, C., Andrews, A. E., Bianco, L., Wilczak, J. M., and Fischer, M. L.: Seasonal variation of CH4 emissions from central California, J. Geophys. Res. Atmos., 117, doi:10.1029/2011JD016896, 2012.

Jeong, S., Hsu, Y.-K., Andrews, A. E., Bianco, L., Vaca, P., Wilczak, J. M., and Fischer, M. L.: A multitower measurement network estimate of California's methane emissions, J. Geophys. Res. Atmos., 118, 11 339–11 351, doi:10.1002/jgrd.50854, 2013.

JRC/PBL: Emission Database for Global Atmosphere Research (EDGAR), release version 4.0, Tech. rep., available at: http://edgar.jrc.ec.europa.eu, last access: 9 September 2015, 2009.

Kirschke, S., Bousquet, P., Ciais, P., Saunois, M., Canadell, J. G., Dlugokencky, E. J., Bergamaschi, P., Bergmann, D., Blake, D. R., Bruhwiler, L., Cameron-Smith, P., Castaldi, S., Chevallier, F., Feng, L., Fraser, A., Heimann, M., Hodson, E. L., Houweling, S., Josse, B., Fraser, P. J., Krummel, P. B., Lamarque, J.-F., Langenfelds, R. L., Le Quere, C., Naik, V., O'Doherty, S., Palmer, P. I., Pison, I., Plummer, D., Poulter, B., Prinn, R. G., Rigby, M., Ringeval, B., Santini, M., Schmidt, M., Shindell, D. T., Simpson, I. J., Spahni, R., Steele, L. P., Strode, S. A., Sudo, K., Szopa, S., van der Werf, G. R., Voulgarakis, A., van Weele, M., Weiss, R. F., Williams, J. E., and Zeng, G.: Three

decades of global methane sources and sinks, Nat. Geosci., 6, 813–823, doi:10.1038/ngeo1955, 2013.

Klevenhusen, F., Bernasconi, S. M., Kreuzer, M., and Soliva, C. R.: Experimental validation of the Intergovernmental Panel on Climate Change default values for ruminant-derived methane and its carbon-isotope signature, Animal Production Science, 51, 974–167, doi:10.1071/AN09112_CO, 2011.

Kort, E. A., Andrews, A. E., Dlugokencky, E., Sweeney, C., Hirsch, A., Eluszkiewicz, J., Nehrkorn, T., Michalak, A., Stephens, B., Gerbig, C., Miller, J. B., Kaplan, J., Houweling, S., Daube, B. C., Tans, P., and Wofsy, S. C.: Atmospheric constraints on 2004 emissions of methane and nitrous oxide in North America from atmospheric measurements and a receptor-oriented modeling framework, Journal of Integrative Environmental Sciences, 7, 125–133, doi:10.1080/19438151003767483, 2010.

Kretschmer, R., Gerbig, C., Karstens, U., Biavati, G., Vermeulen, A., Vogel, F., Hammer, S., and Totsche, K. U.: Impact of optimized mixing heights on simulated regional atmospheric transport of CO_2, Atmos. Chem. Phys., 14, 7149–7172, doi:10.5194/acp-14-7149-2014, 2014.

Kuenen, J. J. P., Visschedijk, A. J. H., Jozwicka, M., and Denier van der Gon, H. A. C.: TNO-MACC_II emission inventory; a multi-year (2003–2009) consistent high-resolution European emission inventory for air quality modelling, Atmos. Chem. Phys., 14, 10963–10976, doi:10.5194/acp-14-10963-2014, 2014.

Manning, A. J., O'Doherty, S., Jones, A. R., Simmonds, P. G., and Derwent, R. G.: Estimating UK methane and nitrous oxide emissions from 1990 to 2007 using an inversion modeling approach, J. Geophys. Res.-Atmos., 116, D02305, doi:10.1029/2010JD014763, 2011.

McKain, K., Down, A., Raciti, S. M., Budney, J., Hutyra, L. R., Floerchinger, C., Herndon, S. C., Nehrkorn, T., Zahniser, M. S., Jackson, R. B., Phillips, N., and Wofsy, S. C.: Methane emissions from natural gas infrastructure and use in the urban region of Boston, Massachusetts, P. Natl. Acad. Sci. USA, 112, 1941–1946, doi:10.1073/pnas.1416261112, 2015.

Meirink, J. F., Bergamaschi, P., and Krol, M. C.: Four-dimensional variational data assimilation for inverse modelling of atmospheric methane emissions: method and comparison with synthesis inversion, Atmos. Chem. Phys., 8, 6341–6353, doi:10.5194/acp-8-6341-2008, 2008.

Michalak, A. M., Hirsch, A., Bruhwiler, L., Gurney, K. R., Peters, W., and Tans, P. P.: Maximum likelihood estimation of covariance parameters for Bayesian atmospheric trace gas surface flux inversions, J. Geophys. Res.-Atmos., 110, D24107, doi:10.1029/2005JD005970, 2005.

Mikaloff Fletcher, S. E., Tans, P. P., Bruhwiler, L. M., Miller, J. B., and Heimann, M.: CH4 sources estimated from atmospheric observations of CH4 and its 13C/12C isotopic ratios: 2. Inverse modeling of CH4 fluxes from geographical regions, Global Biogeochem. Cy., 18, GB4005, doi:10.1029/2004GB002224, 2004.

Miller, S. M., Wofsy, S. C., Michalak, A. M., Kort, E. A., Andrews, A. E., Biraud, S. C., Dlugokencky, E. J., Eluszkiewicz, J., Fischer, M. L., Janssens-Maenhout, G., Miller, B. R., Miller, J. B., Montzka, S. A., Nehrkorn, T., and Sweeney, C.: Anthropogenic emissions of methane in the United States, P. Natl. Acad. Sci. USA, 110, 20018–20022, doi:10.1073/pnas.1314392110, 2013.

Myhre, G., Shindell, D., Bréon, F., Collins, W., Fuglestvedt, J., Huang, J., Koch, D., Lamarque, J., Lee, D., Mendoza, B., Nakajima, T., Robock, A., Stephens, G., Takemura, T., and Zhang, H.: Anthropogenic and Natural Radiative Forcing, in: Climate Change 2013: The Physical Science Basis. Contribution of Working Group I to the Fifth Assessment Report of the Intergovernmental Panel on Climate Change, edited by: Stocker, T., Qin, D., Plattner, G., Tignor, M., Allen, S., Boschung, J., Nauels, A., Xia, Y., Bex, V., and Midgley, P., Cambridge University Press, Cambridge, UK and New York, NY, USA, 659–740, 2013.

Nisbet, E. G., Dlugokencky, E. J., and Bousquet, P.: Methane on the Rise-Again, Science, 343, 493–495, doi:10.1126/science.1247828, 2014.

Nocedal, J. and Wright, S. J.: Numerical optimization, Springer series in operation research and financial engineering, Springer-Verlag, New York, 2006.

Oney, B., Henne, S., Gruber, N., Leuenberger, M., Bamberger, I., Eugster, W., and Brunner, D.: The CarboCount CH sites: characterization of a dense greenhouse gas observation network, Atmos. Chem. Phys. Discuss., 15, 12911–12956, doi:10.5194/acpd-15-12911-2015, 2015.

Owen, J. J. and Silver, W. L.: Greenhouse gas emissions from dairy manure management: a review of field-based studies, Global Change Biology, 21, 550–565, doi:10.1111/gcb.12687, 2015.

Pillai, D., Gerbig, C., Ahmadov, R., Rödenbeck, C., Kretschmer, R., Koch, T., Thompson, R., Neininger, B., and Lavrié, J. V.: High-resolution simulations of atmospheric CO_2 over complex terrain – representing the Ochsenkopf mountain tall tower, Atmos. Chem. Phys., 11, 7445–7464, doi:10.5194/acp-11-7445-2011, 2011.

Ramanathan, V. and Xu, Y.: The Copenhagen Accord for limiting global warming: criteria, constraints, and available avenues, P. Natl. Acad. Sci. USA, 107, 8055–8062, doi:10.1073/pnas.1002293107, 2010.

Rella, C. W., Chen, H., Andrews, A. E., Filges, A., Gerbig, C., Hatakka, J., Karion, A., Miles, N. L., Richardson, S. J., Steinbacher, M., Sweeney, C., Wastine, B., and Zellweger, C.: High accuracy

measurements of dry mole fractions of carbon dioxide and methane in humid air, Atmos. Meas. Tech. Discuss., 5, 5823–5888, doi:10.5194/amtd-5-5823-2012, 2012.

Rödenbeck, C., Houweling, S., Gloor, M., and Heimann, M.: CO2 flux history 1982-2001 inferred from atmospheric data using a global inversion of atmospheric transport, Atmos. Chem. Phys., 3, 1919–1964, doi:10.5194/acp-3-1919-2003, 2003.

Rotach, M. W., Wohlfahrt, G., Hansel, A., Reif, M., Wagner, J., and Gohm, A.: The World is Not Flat: implications for the Global Carbon Balance, B. Am. Meteorol. Soc., 95, 1021–1028, doi:10.1175/BAMS-D-13-00109.1, 2013.

Ruckstuhl, A. F., Henne, S., Reimann, S., Steinbacher, M., Vollmer, M. K., O'Doherty, S., Buchmann, B., and Hueglin, C.: Robust extraction of baseline signal of atmospheric trace species using local regression, Atmos. Meas. Tech., 5, 2613–2624, doi:10.5194/amt-5-2613-2012, 2012.

Schmidt, M., Graul, R., Sartorius, H., and Levin, I.: Carbon dioxide and methane in continental Europe: a climatology, and 222 Radon-based emission estimates, Tellus B, 48, 457–473, doi:10.3402/tellusb.v48i4.15926, 1996.

Schneider, N. and Eugster, W.: Climatic impacts of historical wetland drainage in Switzerland, Climatic Change, 80, 301–321, doi:10.1007/s10584-006-9120-8, 2007.

Schraff, C. H.: Mesoscale data assimilation and prediction of low stratus in the Alpine region, Meteorol. Atmos. Phys., 64, 21–50, doi:10.1007/BF01044128, 1997.

Schroth, M. H., Eugster, W., Gómez, K. E., Gonzalez-Gil, G., Niklaus, P. A., and Oester, P.: Above- and below-ground methane fluxes and methanotrophic activity in a landfill-cover soil, Waste Manage., 32, 879–889, doi:10.1016/j.wasman.2011.11.003, 2012.

Schubert, C. J., Diem, T., and Eugster, W.: Methane Emissions from a Small Wind Shielded Lake Determined by Eddy Covariance, Flux Chambers, Anchored Funnels, and Boundary Model Calculations: a Comparison, Environ. Sci. Technol., 46, 4515–4522, doi:10.1021/es203465x, 2012.

Shindell, D., Kuylenstierna, J. C. I., Vignati, E., van Dingenen, R., Amann, M., Klimont, Z., Anenberg, S. C., Muller, N., Janssens-Maenhout, G., Raes, F., Schwartz, J., Faluvegi, G., Pozzoli, L., Kupiainen, K., Höglund-Isaksson, L., Emberson, L., Streets, D., Ramanathan, V., Hicks, K., Oanh, N. T. K., Milly, G., Williams, M., Demkine, V., and Fowler, D.: Simultaneously Mitigating Near-Term Climate Change and Improving Human Health and Food Security, Science, 335, 183–189, doi:10.1126/science.1210026, 2012.

Stieger, J., Bamberger, I., Buchmann, N., and Eugster, W.: Validation of farm-scale methane emissions using nocturnal boundary layer budgets, Atmos. Chem. Phys. Discuss., 15, 21765–21802, doi:10.5194/acpd-15-21765-2015, 2015.

Stohl, A., Forster, C., Frank, A., Seibert, P., and Wotawa, G.: Technical note: The Lagrangian particle dispersion model FLEXPART version 6.2, Atmos. Chem. Phys., 5, 2461–2474, doi:10.5194/acp-5-2461-2005, 2005.

Stohl, A., Seibert, P., Arduini, J., Eckhardt, S., Fraser, P., Greally, B. R., Lunder, C., Maione, M., Mühle, J., O'Doherty, S., Prinn, R. G., Reimann, S., Saito, T., Schmidbauer, N., Simmonds, P. G., Vollmer, M. K., Weiss, R. F., and Yokouchi, Y.: An analytical inversion method for determining regional and global emissions of greenhouse gases: Sensitivity studies and application to halocarbons, Atmos. Chem. Phys., 9, 1597–1620, doi:10.5194/acp-9-1597-2009, 2009.

Tarantola, A.: Inverse Problem Theory and Methods for Model Parameter Estimation, SIAM, Philadelphia, PA, 2005.

Taylor, K. E.: Summarizing multiple aspects of model performance in a single diagram., J. Geophys. Res.-Atmos., 106, 7183–7192, 2001.

Thompson, R. L. and Stohl, A.: FLEXINVERT: an atmospheric Bayesian inversion framework for determining surface fluxes of trace species using an optimized grid, Geosci. Model Dev., 7, 2223–2242, doi:10.5194/gmd-7-2223-2014, 2014.

Thompson, R. L., Gerbig, C., and Rödenbeck, C.: A Bayesian inversion estimate of N_2O emissions for western and central Europe and the assessment of aggregation errors, Atmos. Chem. Phys., 11, 3443–3458, doi:10.5194/acp-11-3443-2011, 2011.

Thompson, R. L., Stohl, A., Zhou, L. X., Dlugokencky, E., Fukuyama, Y., Tohjima, Y., Kim, S. Y., Lee, H., Nisbet, E. G., Fisher, R. E., Lowry, D., Weiss, R. F., Prinn, R. G., O'Doherty, S., Young, D., and White, J. W. C.: Methane emissions in East Asia for 2000–2011 estimated using an atmospheric Bayesian inversion, J. Geophys. Res.-Atmos., 120, 4352–4369, doi:10.1002/2014JD022394, 2015.

Tiedtke, M.: A Comprehensive Mass Flux Scheme for Cumulus Parameterization in Large-Scale Models, Mon. Weather Rev., 117, 1779–1800, doi:10.1175/1520-0493(1989)117<1779:ACMFSF>2.0.CO;2, 1989.

Tolk, L. F., Meesters, A. G. C. A., Dolman, A. J., and Peters, W.: Modelling representation errors of atmospheric CO_2 mixing ratios at a regional scale, Atmos. Chem. Phys., 8, 6587–6596, doi:10.5194/acp-8-6587-2008, 2008.

Turner, A. J., Jacob, D. J., Wecht, K. J., Maasakkers, J. D., Lundgren, E., Andrews, A. E., Biraud, S. C., Boesch, H., Bowman, K. W., Deutscher, N. M., Dubey, M. K., Griffith, D. W. T., Hase, F., Kuze, A., Notholt, J., Ohyama, H., Parker, R., Payne, V. H., Sussmann, R., Sweeney, C., Velazco, V. A., Warneke, T., Wennberg, P. O., and Wunch, D.: Estimating global and North Amer-

ican methane emissions with high spatial resolution using GOSAT satellite data, Atmos. Chem. Phys., 15, 7049–7069, doi:10.5194/acp-15-7049-2015, 2015.

Tuzson, B., Hiller, R. V., Zeyer, K., Eugster, W., Neftel, A., Ammann, C., and Emmenegger, L.: Field intercomparison of two optical analyzers for CH_4 eddy covariance flux measurements, Atmos. Meas. Tech., 3, 1519–1531, doi:10.5194/amt-3-1519-2010, 2010.

Tuzson, B., Henne, S., Brunner, D., Steinbacher, M., Mohn, J., Buchmann, B., and Emmenegger, L.: Continuous isotopic composition measurements of tropospheric CO_2 at Jungfraujoch (3580 m a.s.l.), Switzerland: real-time observation of regional pollution events, Atmos. Chem. Phys., 11, 1685–1696, doi:10.5194/acp-11-1685-2011, 2011.

Vermeulen, A. T., Eisma, R., Hensen, A., and Slanina, J.: Transport model calculations of NW-European methane emissions, Environ. Sci. Policy, 2, 315–324, doi:10.1016/S1462-9011(99)00021-0, 1999.

Vogelezang, D. H. P. and Holtslag, A. A. M.: Evaluation and model impacts of alternative boundary-layer height formulations, Boundary-Layer Meteorology, 81, 245–269, doi:10.1007/BF02430331, 1996.

Wecht, K. J., Jacob, D. J., Frankenberg, C., Jiang, Z., and Blake, D. R.: Mapping of North American methane emissions with high spatial resolution by inversion of SCIAMACHY satellite data, J. Geophys. Res.-Atmos., 119, 7741–7756, doi:10.1002/2014JD021551, 2014.

Wennberg, P. O., Mui, W., Wunch, D., Kort, E. A., Blake, D. R., Atlas, E. L., Santoni, G. W., Wofsy, S. C., Diskin, G. S., Jeong, S., and Fischer, M. L.: On the Sources of Methane to the Los Angeles Atmosphere, Environ. Sci. Technol., 46, 9282–9289, doi:10.1021/es301138y, 2012.

Wüst-Galley, C., Grünig, A., and Leifeld, J.: Locating Organic Soils for the Swiss Greenhouse Gas Inventory, Tech. rep., Agroscope, 2015.

Zavala-Araiza, D., Lyon, D. R., Alvarez, R. A., Davis, K. J., Harriss, R., Herndon, S. C., Karion, A., Kort, E. A., Lamb, B. K., Lan, X., Marchese, A. J., Pacala, S. W., Robinson, A. L., Shepson, P. B., Sweeney, C., Talbot, R., Townsend-Small, A., Yacovitch, T. I., Zimmerle, D. J., and Hamburg, S. P.: Reconciling divergent estimates of oil and gas methane emissions, Proceedings of the National Academy of Sciences, 112, 15 597–15 602, doi:10.1073/pnas.1522126112, 2015.

Zeitz, J. O., Soliva, C. R., and Kreuzer, M.: Swiss diet types for cattle: how accurately are they reflected by the Intergovernmental Panel on Climate Change default values?, Journal of Integrative Environmental Sciences, 9, 199–216, doi:10.1080/1943815X.2012.709253, 2012.

Zellweger, C., Forrer, J., Hofer, P., Nyeki, S., Schwarzenbach, B., Weingartner, E., Ammann, M., and Baltensperger, U.: Partitioning of reactive nitrogen (NO_y) and dependence on meteorological

conditions in the lower free troposphere, Atmos. Chem. Phys., 3, 779–796, doi:10.5194/acp-3-779-2003, 2003.

Zhao, C., Andrews, A. E., Bianco, L., Eluszkiewicz, J., Hirsch, A., MacDonald, C., Nehrkorn, T., and Fischer, M. L.: Atmospheric inverse estimates of methane emissions from Central California C8 - D16302, J. Geophys. Res. Atmos., 114, D16 302, doi:10.1029/2008JD011671, 2009.

Table 1. Overview of the location of the observational sites used in the study, including particle release heights as used in FLEXPART simulations. See text for details on release height selection.

Station	ID	Longitude (° E)	Latitude (° N)	Altitude (m a.s.l.)	COSMO-7 height (m a.s.l.)	Inlet height (m)	low release (m)	high release (m)
Beromünster	BEO	8.1755	47.1896	797	615	212	212 a.g.l.	1014 a.s.l.
Lägern Hochwacht	LHW	8.3973	47.4822	840	492	32	150 a.g.l.	250 a.g.l.
Schauinsland	SSL	7.9167	47.9000	1205	750	10	980 a.s.l.[a]	–
Jungfraujoch	JFJ	7.9851	46.5475	3580	2650	3	3100 a.s.l.[b]	–
Früebüel	FRU	8.5378	47.1158	982	711	5	50 a.g.l.	982 a.s.l.
Gimmiz	GIM	7.2480	47.0536	443	496	32	32 a.g.l.	–

[a] 920 m a.s.l. in FLEXPART-ECMWF
[b] 3000 m a.s.l. in FEXPART-ECMWF

Table 2. Set-up of the base (B) and sensitivity inversions (S-X).

Inversion	Method	FLEXPART version	Sites	Baseline method	Seasonality	Prior emissions	Model/Observation uncertainty
B	Bayesian	COSMO	BEO, LHW, JFJ, SSL	Single	N	MAIOLICA	standard
S-V	Bayesian	COSMO	BEO, LHW, JFJ, SSL	Single	Y	MAIOLICA	standard
S-K	extKF	COSMO	BEO, LHW, JFJ, SSL	Single	Y	MAIOLICA	standard
S-EC	Bayesian	ECMWF	BEO, LHW, JFJ, SSL	Single	N	MAIOLICA	standard
S-T	Bayesian	COSMO	BEO, LHW, JFJ, SSL	Single	N	TNO/MACC-2	standard
S-E	Bayesian	COSMO	BEO, LHW, JFJ, SSL	Single	N	EDGAR	standard
S-S	Bayesian	COSMO	BEO, LHW, JFJ, SSL	Single	N	MAIOLICA	Stohl
S-ML	Bayesian	COSMO	BEO, LHW, JFJ, SSL	Single	N	MAIOLICA	ML
S-O1	Bayesian	COSMO	BEO	Single	N	MAIOLICA	standard
S-O2	Bayesian	COSMO	LHW	Single	N	MAIOLICA	standard
S-O3	Bayesian	COSMO	BEO LHW	Single	N	MAIOLICA	standard
S-O4	Bayesian	COSMO	BEO, LHW, JFJ, SSL, FRU	Single	N	MAIOLICA	standard
S-O5	Bayesian	COSMO	BEO, LHW, JFJ, SSL, FRU, GIM	Single	N	MAIOLICA	standard
S-B1	Bayesian	COSMO	BEO, LHW, JFJ, SSL	Gradient	N	MAIOLICA	standard
S-B2	Bayesian	COSMO	BEO, LHW, JFJ, SSL	Grid	N	MAIOLICA	standard

Table 3. Overview of parameters used for the construction of the uncertainty covariance matrices: contributions to model/observation uncertainty σ_{min} and σ_{srr}, baseline uncertainty factor f_{b}, baseline correlation length τ_{b}, prior correlation length L and prior Swiss emission uncertainty σ_{E}.

	σ_{min} (nmol mol^{-1})				σ_{srr} (–)				f_{b} (–)				τ_{b} (d)	L (km)	σ_{E} (%)
	BEO	LHW	SSL	JFJ	BEO	LHW	SSL	JFJ	BEO	LHW	SSL	JFJ			
Base inversion (B-B)															
low	11	16	11	17	0.53	0.47	0.34	0.36	1	1	1	1	14	50	16
high	22	23	11	17	0.45	0.46	0.35	0.36	1	1	1	1	14	50	16
ECMWF inversion (S-EC)															
low	1	21	11	17	0.76	0.45	0.34	0.35	1	1	1	1	14	50	16
high	14	22	11	17	0.52	0.45	0.35	0.35	1	1	1	1	14	50	16
Stohl09 (S-S)															
low	40	41	22	20	0	0	0	0	1	1	1	1	14	50	16
high	41	44	22	20	0	0	0	0	1	1	1	1	14	50	16
Maximum likelihood (S-ML)															
low	25	24	19	20	0.78	0.76	0.54	1.24	3.6	5.1	2.1	2.0	19	50	31
high	39	35	19	20	0.64	0.63	0.54	1.23	4.2	5.5	2.4	2.4	23	51	30
Extended Kalman Filter (S-K)															
low	14	14	14	14	0.5	0.5	0.5	0.5	–	–	–	–	–	50	16
high	14	14	14	14	0.5	0.5	0.5	0.5	–	–	–	–	–	50	16

Table 4. Overview of results of sensitivity inversions. E_A and E_B are the total Swiss CH_4 prior and posterior emissions (Gg yr^{-1}), respectively, and S is the posterior Taylor skill score for the individual sites. The settings of the sensitivity inversions are given in Table 2.

Inversion	Emissions		Skill score (S)					
	prior E_A	posterior E_B	BEO	LHW	SSL	JFJ	FRU	GIM
B low	183.0 ± 29.3	179.0 ± 7.0	0.83	0.89	0.91	0.78	0.77	0.50
B high	183.0 ± 29.3	195.0 ± 7.3	0.84	0.86	0.91	0.78	0.74	0.51
S-V low	183.0 ± 29.3	185.9 ± 6.5	0.84	0.89	0.91	0.77	0.77	0.51
S-V high	183.0 ± 29.3	197.3 ± 6.7	0.85	0.86	0.91	0.78	0.75	0.53
S-K low	179.6 ± 28.7	193.1 ± 13	0.92	0.94	0.94	0.84	–	–
S-K high	179.6 ± 28.7	216.7 ± 14	0.93	0.95	0.94	0.85	–	–
S-EC low	184.4 ± 28.0	171.1 ± 8.0	0.79	0.87	0.91	0.77	0.74	0.29
S-EC high	184.5 ± 29.0	182.1 ± 7.6	0.88	0.87	0.92	0.77	0.74	0.31
S-T low	188.1 ± 30.1	180.3 ± 7.2	0.82	0.89	0.91	0.78	0.74	0.44
S-T high	187.7 ± 29.7	199.1 ± 7.4	0.83	0.87	0.91	0.78	0.69	0.46
S-E low	228.2 ± 36.5	184.3 ± 7.9	0.84	0.89	0.90	0.77	0.75	0.43
S-E high	227.4 ± 36.4	207.1 ± 7.9	0.83	0.88	0.90	0.77	0.69	0.46
S-S low	183.3 ± 29.3	169.3 ± 7.5	0.79	0.84	0.89	0.77	0.70	0.39
S-S high	183.3 ± 29.3	197.6 ± 8.0	0.81	0.84	0.89	0.77	0.70	0.51
S-ML low	183.0 ± 37.3	158.4 ± 13	0.84	0.92	0.90	0.78	0.73	0.44
S-ML high	183.0 ± 65.6	168.7 ± 13	0.85	0.91	0.89	0.78	0.66	0.44
S-O1 low	184.9 ± 29.2	183.3 ± 10	0.85	0.83	0.84	0.62	0.78	0.40
S-O1 high	184.6 ± 29.5	200.8 ± 11	0.87	0.81	0.84	0.63	0.78	0.38
S-O2 low	185.8 ± 29.7	214.3 ± 11	0.77	0.90	0.83	0.66	0.77	0.57
S-O2 high	184.5 ± 29.6	229.6 ± 11	0.75	0.88	0.82	0.66	0.76	0.64
S-O3 low	183.3 ± 29.3	198.5 ± 7.9	0.85	0.91	0.84	0.66	0.79	0.49
S-O3 high	183.5 ± 29.4	221.3 ± 8.3	0.86	0.89	0.83	0.66	0.78	0.51
S-O4 low	183.3 ± 28.3	191.2 ± 6.2	0.84	0.90	0.91	0.78	0.82	0.46
S-O4 high	183.3 ± 29.2	207.7 ± 6.5	0.85	0.88	0.91	0.79	0.85	0.48
S-O5 low	181.9 ± 29.1	208.8 ± 6.0	0.84	0.90	0.92	0.79	0.83	0.66
S-O5 high	181.9 ± 29.1	224.3 ± 6.1	0.85	0.88	0.91	0.79	0.85	0.69
S-B1 low	183.0 ± 29.3	194.0 ± 6.9	0.83	0.89	0.92	0.79	0.77	0.49
S-B1 high	183.0 ± 29.3	211.7 ± 7.2	0.84	0.87	0.92	0.79	0.74	0.51
S-B2 low	183.0 ± 29.3	195.1 ± 6.9	0.88	0.89	0.92	0.83	0.82	0.62
S-B2 high	183.0 ± 29.3	223.6 ± 6.9	0.88	0.88	0.92	0.83	0.75	0.69

Table 5. Swiss CH_4 emissions ($Gg\,yr^{-1}$) by most relevant source process as reported by FOEN to UNFCCC for the year 2012 and total emissions as estimated by this study. Uncertainties denote 1σ confidence levels.

Source	SGHGI 2014	SGHGI 2015	This study
Total	176 ± 28	206 ± 33	197 ± 19
1A Fuel combustion	4.1	3.7	
1B Fugitive emissions from fuels	8.1	8.4	
2 Industrial processes	0.1	0.1	
3A Enteric fermentation	118.9	130.5	
3B Manure management	30.8	31.0	
5A Solid waste disposal on land	7.5	8.5	
5B Biological treatment of waste[a]	5.4	16.7	
5C Waste incineration[b]	0.3	0.3	
5D Waste water handling	0.4	6.8	

[a] composting and anaerobic digestion.
[b] without municipal solid waste incineration.

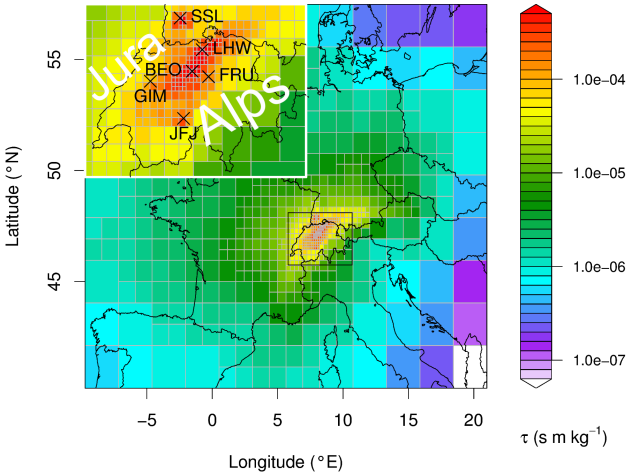

Figure 1. Total source sensitivity for the period March 2013 to February 2014 and the 4 sites used in the base inversion (crosses and labels in subplot; BEO: Beromünster, LHW: Lägern, JFJ: Jungfraujoch, SSL: Schauinsland). Source sensitivities are displayed on the reduced resolution grid that is used in the inversion. The units of the source sensitivity are given as residence times divided by atmospheric density and surface area. The locations of the two validation sites (FRU: Früebüel and GIM: Gimmiz) are given in the subplot as well.

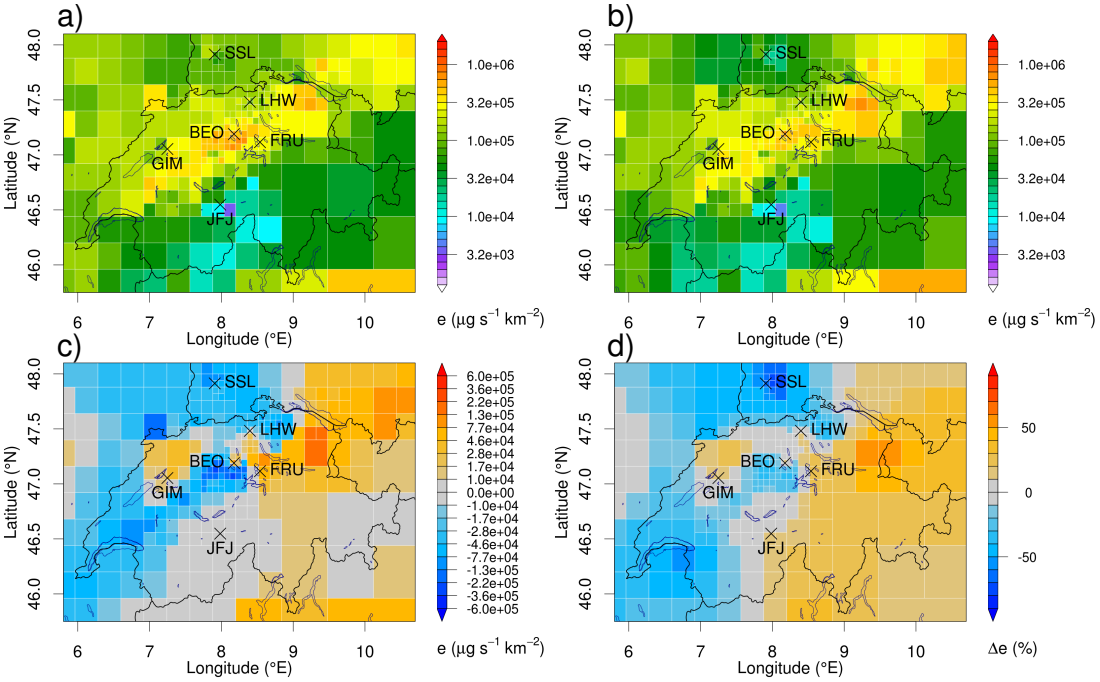

Figure 2. (a) prior and **(b)** posterior surface fluxes of CH_4 in the base inversion and low particle release heights (B low). **(c)** absolute and **(d)** relative (to prior) difference between posterior and prior emission fluxes. For panels c and d red (blue) colors indicate higher (lower) posterior than prior emissions.

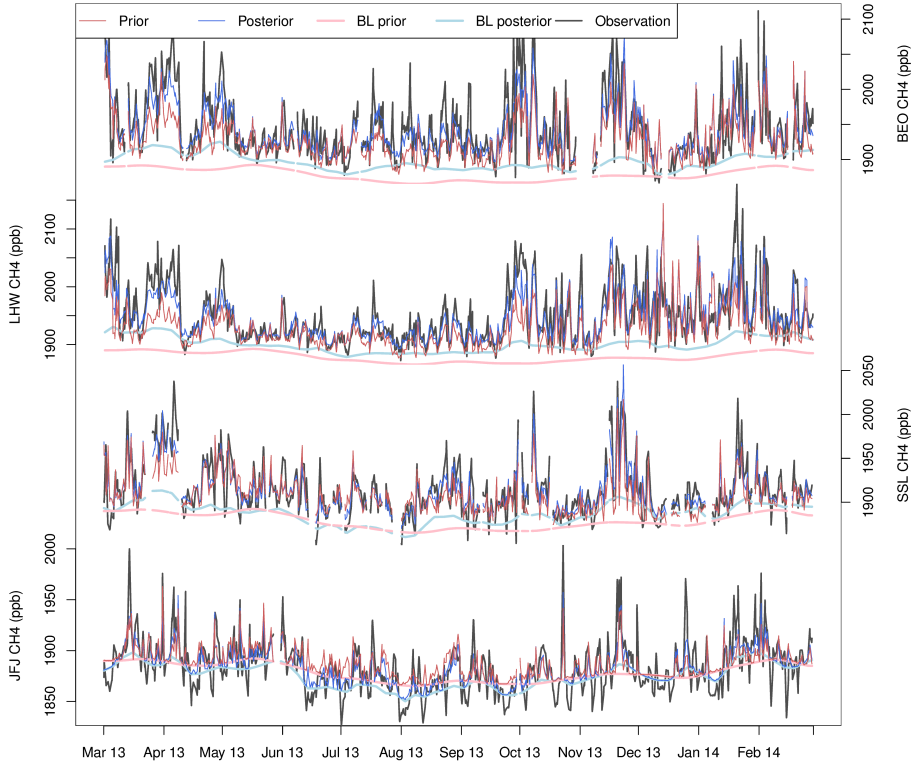

Figure 3. Observed (black) and simulated (prior: red; posterior: blue) CH_4 time series in the base inversion with low release heights (B low) at sites used in the inversion. Also given are the baseline mole fractions as used in the simulations (prior: light red; posterior: light blue). Note that the y axes were scaled for each site separately. All data represent 3-hourly averages.

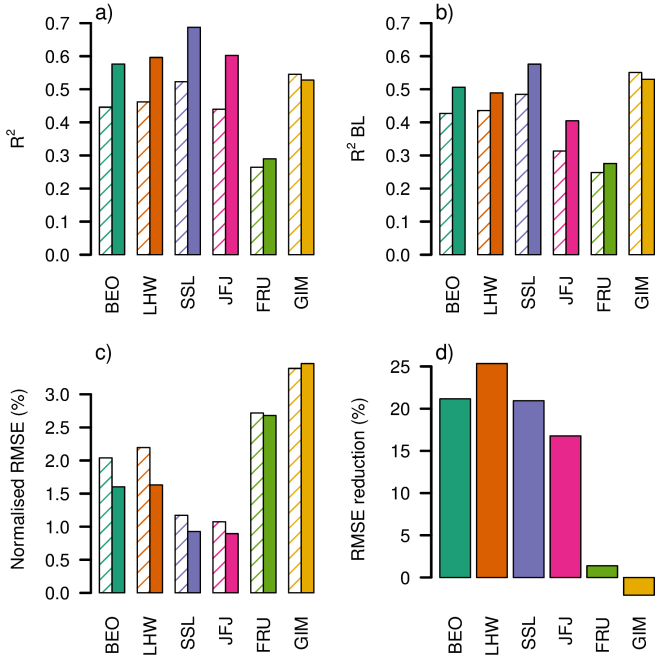

Figure 4. Model performance parameters for simulated time series at all sites for the base inversion with low particle release heights (B low): prior (shaded) and posterior (filled). **(a)** coefficient of determination (R^2) for complete signal and **(b)** above baseline signal, **(c)** normalised RMSE and **(d)** reduction of RMSE between prior and posterior. Note that the FRU and GIM sites were only used for validation but not in the inversion. All comparison statistics are based on 3-hourly averages.

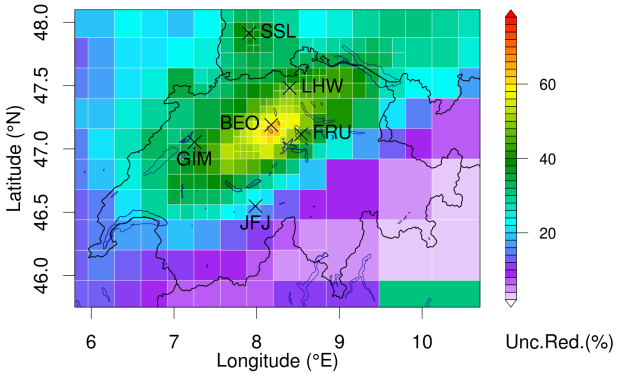

Figure 5. Uncertainty reduction between prior and posterior fluxes given in % relative to prior uncertainty ($1 - \sigma_B/\sigma_A$) for the base inversion with low partice release height.

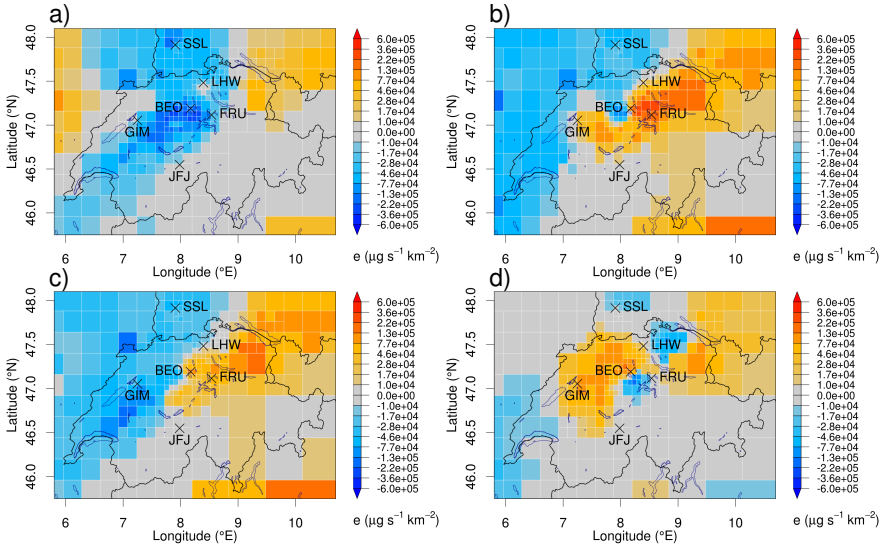

Figure 6. Absolute difference between posterior minus prior emission fluxes for seasonal inversion. **(a)** December, January, February, **(b)** March, April, May, **(c)** June, July, August, **(d)** September, October, November.

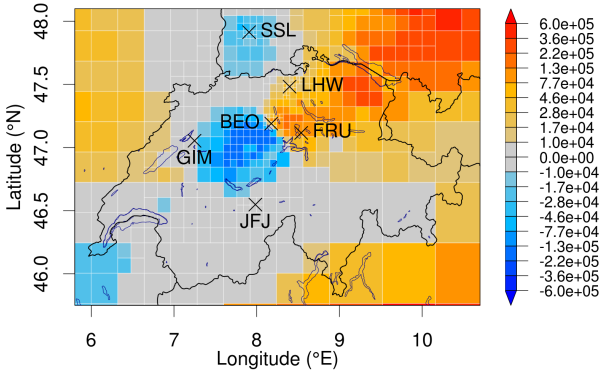

Figure 7. Absolute difference between posterior minus prior emission fluxes as obtained from extended Kalman filter inversion with low particle releases.

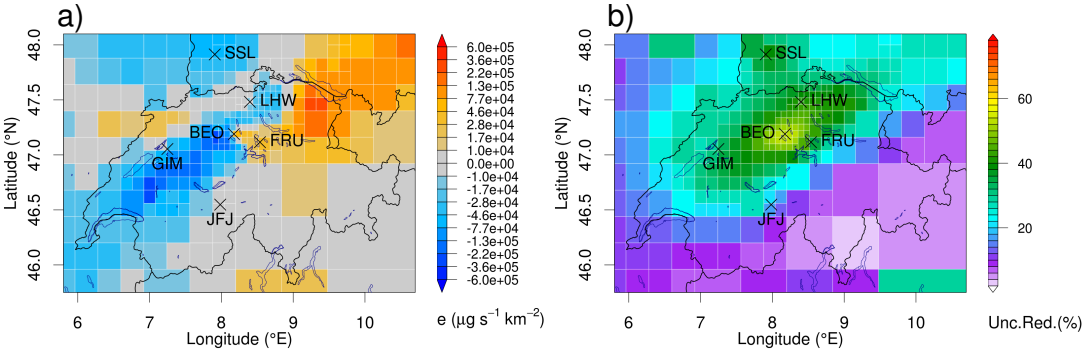

Figure 8. (a) Absolute difference between posterior minus prior emission fluxes for S-EC with low particle release height. **(b)** Uncertainty reduction between prior and posterior fluxes given in % relative to prior uncertainty ($1 - \sigma_B/\sigma_A$).

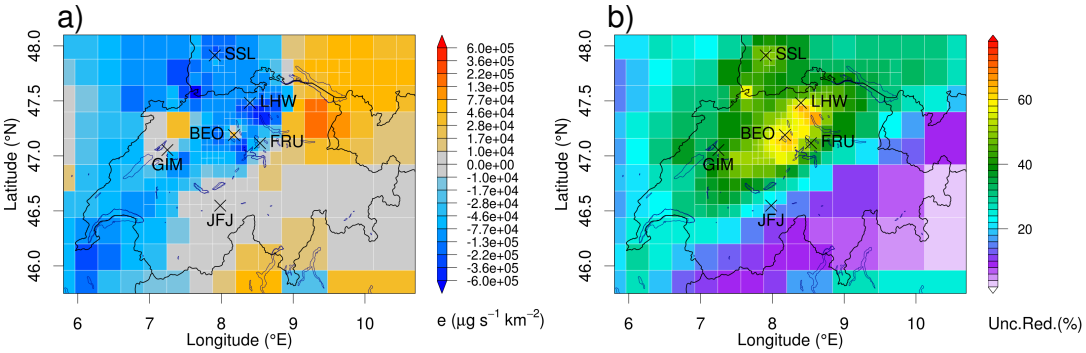

Figure 9. Absolute difference between posterior minus prior emission fluxes when using EDGAR instead of MAIOLICA prior fluxes.

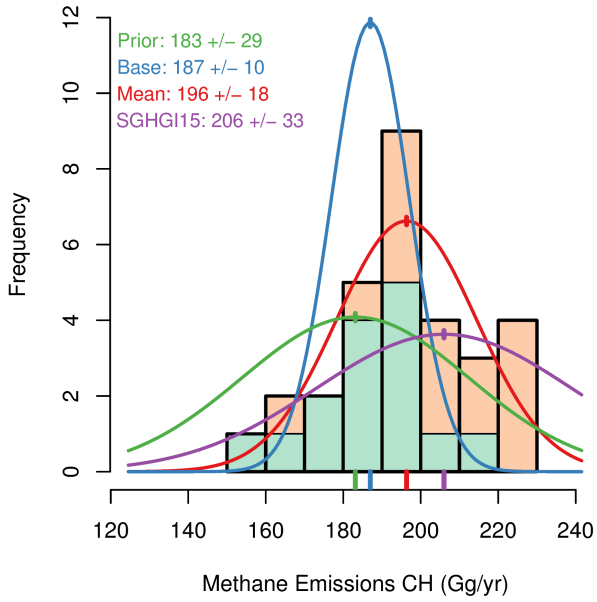

Figure 10. Histogram of total Swiss CH_4 emissions taken from all individual sensitivity inversions: low (light green) and high (light orange) particle releases. The base inversion prior (green) and posterior (blue) estimate as well as the average over all sensitivity inversions (red) and the SGHGI 2015 estimate (purple) are indicated by their Gaussian probability density functions.